University of Alberta

Measuring Energy Transfer from Wildland Forest Fires

by

Erik Arthur Sullivan

A thesis submitted to the Faculty of Graduate Studies and Research
in partial fulfillment of the requirements for the degree of

Master of Science

Department of Mechanical Engineering

Spring 2014
Edmonton, Alberta

ABSTRACT

Current practices for measuring high heat flux, in scenarios such as wildland forest fires, are to utilize expensive, thermopile-based sensors, coupled with mathematical models based on a semi-infinite length-scale. While these sensors are acceptable for experimental testing in laboratories, high errors or needs for water-cooling limits their applications in field experiments. Therefore, a one-dimensional, finite-length scale, transient heat conduction model was developed and combined with an inexpensive, thermocouple-based rectangular sensor to create a rapidly deployable, non-cooled sensor for testing in field environments. Constant heat flux, tree burning tests, and a surface fire field experiment were conducted to validate the proposed analytical model and test the sensor in simulated and real fire settings. The proposed heat flux measurement method provided results similar to those obtained from a commercial heat flux gauge, to within one standard deviation. This suggests that the use of a finite-length scale model, coupled with an inexpensive thermocouple-based sensor, is effective in estimating the intense heat loads from wildland fires.

ACKNOWLEDGEMENTS

I would like to start with thanking my supervisor, Dr. André McDonald. Without his support and guidance during my graduate studies, this thesis would not be possible. He made it an enjoyable experience where I gained a lot of knowledge and practical skills preparing me for a successful career in industry.

I would also like to thank Mr. Stephen Paskaluk, Mr. Mark Ackerman, and FP Innovations for their assistance in collecting, assembling, and providing the use of the radiant panel and the Protective Clothing and Equipment Research Facility (PCERF) to collect the experimental data used in this study. I would also like to thank Chelsea Horton for the abundance of help while writing and providing me with good conversation when I needed to be distracted. Furthermore, I would like to thank Connor Hall for reviewing my thesis and his willingness to engage in enjoyable coffee conversations.

I would like to thank everyone from Room 6-25. I would like to thank Natanael Melendez and David Therrien for helping me with administrative tasks and basic theoretical questions during the early stages of my masters. In addition, I would like to thank Hossein Ashrafizadeh for assisting me with the thermal spray torch and robot.

Last, but certainly not least, I would like to thank my family for being supportive of my decision and encouraging me to advance my education.

TABLE OF CONTENTS

LIST OF FIGURES

LIST OF TABLES

NOMENCLATURE AND ABBREVIATIONS

i. List of Symbols

A,B,C integration constants

Bi Biot number

$$\mathrm{Bi} = \frac{hL}{k}$$

C_p specific heat capacity ($J\text{-}g^{-1}\text{-}°C^{-1}$)

d location of embedded thermocouple (m)

g gravity, 9.81 m s^{-2}

h convective heat transfer coefficient ($W\ m^{-2}\ °C^{-1}$)

$\bar{h}$ average convective heat transfer coefficient ($W\ m^{-2}\ °C^{-1}$)

H height of slab (m)

k thermal conductivity ($W\ m^{-1}\ °C^{-1}$)

L slab thickness (m)

Pr Prandtl number

$$\mathrm{Pr} = \frac{\upsilon}{\alpha}$$

q'' heat flux ($W\ m^{-2}$)

Ra Rayleigh number

$$\mathrm{Ra}_H = \frac{g\beta(T_s - T_o)H^3 \,\mathrm{Pr}}{\upsilon^2}$$

T temperature (^oC)

t time (s)

W width of slab (m)

x spatial co-ordinate variable

X variable dependent on x, only

ii. Greek Symbols

α thermal diffusivity ($m^2\ s^{-1}$)

β compressibility factor (K^{-1})

ε emissivity

λ separation constant (m^{-1})

ρ density ($kg\text{-}m^{-3}$)

σ Stefan-Boltzmann constant, $5.67 \times 10^{-8}\ Wm^{-2}K^{-4}$

τ variable dependent on t, only

υ kinematic viscosity ($m^2\ s^{-1}$)

Φ function dependent on x, only

Ψ	function dependent on x and t
ω	error variable
∞	ambient

iii. Subscripts

1	temperature at $x = L$
f	film of air
i	initial
n	summation index
s	surface

v. List of Abbreviations

DFT	Directional Flame Thermometer
HFG	Hemispherical Heat Flux Gauge
QPL	Qualified Products List
VOCs	Volatile Organic Compounds

1. INTRODUCTION

1.1 Wildland Forest Fires

Forest fires have been increasing in frequency due to climate change factors such as increased temperatures, variability in moisture conditions, forest disturbances such as insects, and communities that expand into wildland urban interface environments [1–3]. Residential settling near these interfaces increases the likelihood of forest fire ignition, fire damage, and can threaten the safety of its occupants [4]. Consequently, annual suppression costs have exceeded $1 billion dollars in the United States alone, and are expected to increase in the future [5, 6]. Recent trends toward warmer, drier summers are expected to increase the amount of forest fires globally [7]. Of particular interest are the fires that occurred recently in Kelowna, BC and Slave Lake, AB where over 650 homes were lost, 48,000 hectares were burned, and over $730 million dollars in damages were incurred [8, 9]. Therefore, research on the energy exchange between wildland forest fires and the surroundings is crucial in the prevention and suppression of wildfires, validation of fire models, development of codes, prediction of fire effects, and insight into firefighter safety.

Forest fires have occurred on Earth for millions of years and play an important role in the structure and function of our ecosystems [10]. They can occur naturally by lightning, volcanoes or spontaneously ignited coal seams but,

more often than not, they are started by humans [10, 11]. Of particular interest are the fires that endanger the lives of people and structures which gain particular interest and are usually featured in the media. These fires become high priority and are usually met with the greatest man power to try to extinguish them. Firefighters work diligently to contain these fires using suppression chemicals before the fire can reach nearby communities and before the fire becomes a crown fire.

Crown fires are just one of the three types of fires that occur in wildland forests. There are also ground and surface fires as shown in Fig. 1-1 [12]. Ground fires burn underneath the surface by smoldering combustion, while surface fires are combustion of fuels near the surface such as grass, shrubs, leaves, tree limbs, and forest needles [12]. Crown fires burn through the top of the trees and are associated with extreme fire behaviour, implying an increase in the rate of spread, intensity, flame length, and spotting [12, 13]. When fires become crown fires, they are commonly considered out of control due to the severe fire behaviour. In addition, wind becomes a dominant influence on the fire direction and intensity because the fire is now in the canopy of the trees [12]. This makes it difficult to predict fire direction and thus adds to the already complicated fire suppression tactics. The last important variable in forest fires is vegetation. Vegetation has an extensive impact on the fire intensity due to the various fuel types found in forests and their respective flammability characteristics.

Figure 1-1: Fire types in wildland forests: (a) ground fire, (b) surface fire, and (c) crown fire

1.2 Fuel Types

With the vast amount of forests globally, the vegetation that grows within them is diverse and ever changing. Additionally, factors including the size, shape, compactness, arrangement, moisture content, and quantity all play a role in the intensity of the fire [12]. To distinguish the differences in fuels, there are three categories that are used to differentiate among vegetative fuels: aerial fuels, surface fuels, and ground fuels (as shown in Fig. 1-2). Aerial fuels consist of trees, tree branches, moss, and snags while surface fuels consist of low vegetation, large logs, leaves, and grass. Ground fuels consist of roots and duff (fermentation and humus layers of the forest floor) [12]. The compactness of ground fuels

causes a slow fire spread rate, but is important because many fires that appear to be extinguished can be restarted by a slow moving ground fire.

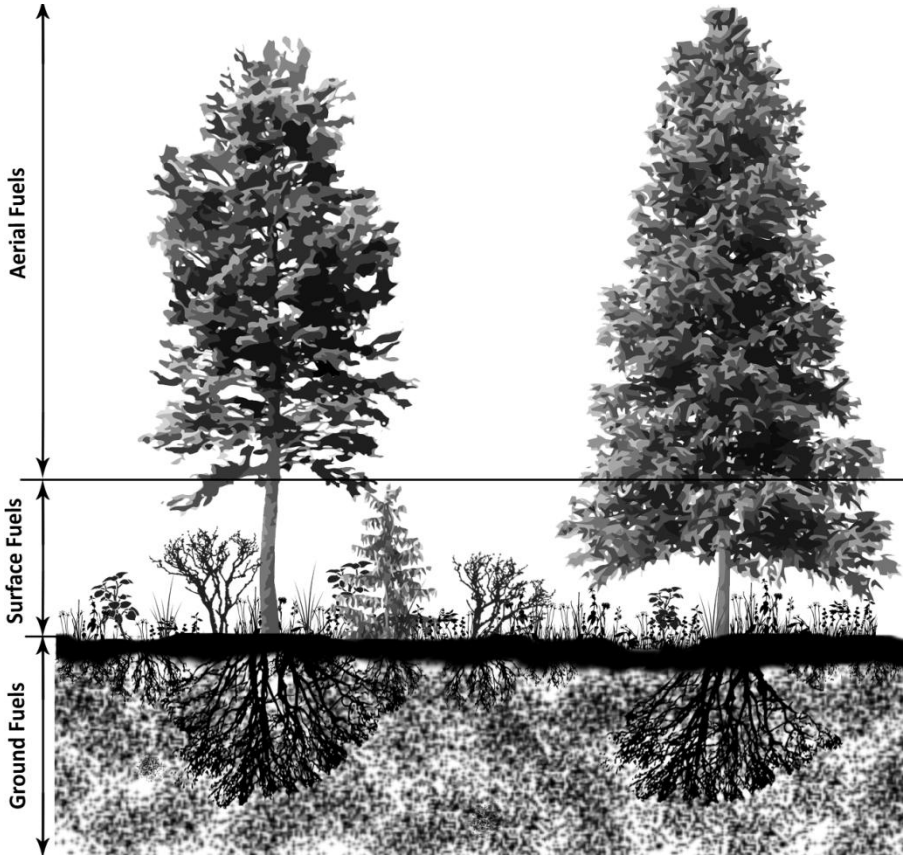

Figure 1-2: Categories of vegetative fuel types [14]

All three types of forest fires, especially crown fires, pose a danger to structures and their occupants due to the immense amount of energy that they transfer to the surroundings. Thus, measuring this energy exchange is crucial in determining occupant safety, as well as minimizing the damage on buildings. Currently, limited data is available on heat flux estimates from wildland forest

fires due to the scarcity of field-ready heat flux meters. Having such sensors would allow the collection of valuable data that would provide insight into the design of heat-resistant building materials, testing of various fuel treatments, and the development of new safety codes.

1.3 Measurement of Energy from Forest Fires

1.3.1 Current industry methods

There are many different methods that have been developed in an attempt to quantify the energy released from a fire as shown in the work of Kremens et al. [15]. The shortfall of the available methods presented in the open literature is the requirement of multiple measurements at a large scale, which are difficult to obtain and severely limits the accuracy of model predictions [15]. One common method to measure the intensity of a forest fire is to use Byram's fireline intensity [16]. Bryam's fireline intensity is the rate of heat release per unit time per unit length of fire front and is measured in $kW\text{-}m^{-1}$ [17]. The fire front, also known as the fireline, is the fastest-spreading part of the perimeter of the fire [12]. Fireline intensity represents the radiant and convective energy of the flame front, knowledge of which is essential for suppression activities because it incorporates several factors of the fire environment into a single parameter number [17, 18]. It is presented in the scientific literature and by members in the forest fire industry as the best measure of forest fire intensity but only a small number of methods

have been developed to measure it [19]. They use these intensities to rank a fire from 1 to 6, based on work from Taylor et al. [20] for a fire behaviour prediction system, where a class 1 fire is a smoldering surface fire with an intensity of less than 10 kW-m^{-1} while a class 6 fire is a blow-up or conflagration with an intensity of greater than 10,000 kW-m^{-1} [20]. Although this is a good indication of fire behaviour, it can be misleading because it does not correlate to the exact energy that an object may experience within the fire. Therefore, using other techniques to measure energy release and transfer in terms of heat flux (in kW-m^{-2}) is more useful to fire scientists [18]. Heat flux is the rate at which energy is transferred (released or absorbed) per unit area perpendicular to the direction of transfer. This energy can be transferred by conduction, convection, and/or radiation [21, 22]. For example, measuring heat flux, instead of fireline intensity, supplies a researcher with a single number they can then replicate in devices such as a mass loss cone calorimeter for the testing of materials or products. In addition, fire scientists can take heat flux data and directly correlate it to a type of burn a person would receive. For instance, heat fluxes of 2, 10, and 50 kW-m^{-2} would cause a second-degree skin burn in 48, 4.3 and 0.42 s, respectively [23]. For this reason, fireline intensity is not as useful as heat flux because it is difficult to relate fireline intensity to the specific amount of energy to which an object will be exposed. This will aid in the design of fire resistant materials or establish set-back distances with regards to building codes.

In high heat flux situations such as forest fires, the measurement of energy transfer can be inhibited by the lack of simple, durable, affordable, portable, and

high performance instruments [24, 25]. In industry, thermocouples are placed in a straight line, perpendicular to the fireline to measure air temperature while the fire is burning. Although, these are used to measure the time of arrival of the flame front and completion of flaming combustion, Butler et al. [26] has shown that these air temperature measurements do not correlate with the radiant energy transfer and does not accurately quantify the amount of preheating by thermal radiation that occurs prior to arrival of the flame front, which is essential in the design of heat resistant materials and setback distances in housing development standards. This has motivated the fabrication of a custom thermocouple-based sensor that is capable of measuring high heat fluxes for an extended period of time. A similar sensor was developed using thermocouples and an asbestos-based material. A semi-infinite similarity transformation heat transfer method was used to estimate the fluxes, but errors would increase beyond 60 seconds of measurement due to excessive backside temperatures in the sensor [27]. Furthermore, since temperature gradients develop inside the sensors, a cooling time was required between each subsequent test, severely limiting their potential use in forest fire scenarios [28]. This deficiency has led to the need for a simple sensor fabricated from a high thermal conductivity material that uses a finite-length scale heat transfer model to increase the measuring time during experiment and field testing.

In an effort to expand heat flux data collection opportunities in wildland fires, other non-cooled instrumentation has been studied and developed by other researchers [29–36]. One non-cooled device that is available is a hemispherical

heat flux gauge (HFG). This gauge is fabricated by compressing a thermocouple between two thin stainless steel plates with the front side exposed to incident heat flux and the back side insulated by ceramic fiber insulation. The experimental temperature data is then used in a two-layer, planar wall heat conduction problem to solve for the unknown heat flux [32]. As shown by Lam and Weckman [32], the HFG produced significantly lower heat flux estimates when compared to the Schmidt-Boelter gauge and it was concluded that there are flaws in the sensor design. Another non-cooled heat flux device investigated by researchers was a directional flame thermometer (DFT) [29–33]. This sensor consists of two thin metal plates separated by a composite material with one thermocouple attached to each plate and does not require external cooling [29]. An inverse heat conduction model is then employed to estimate the heat flux between the plates [29]. While inverse heat conduction, linked to a DFT is a powerful methodology, this thesis study expands upon the ideas of Keltner et al. [29] by focusing attention on the use of simpler materials and a simple model that requires less computer processing.

1.3.2 Mathematical models

Typical transient heat transfer models used to estimate temperature distributions and heat fluxes in high heat load applications tend to use inverse heat transfer methods applied over semi-infinite length scales, or use Green's functions [37–43]. However, these methods add mathematical complexity in the estimation

of heat flux and require numerical techniques for their solution [38, 40]. Consequently, a simplified heat transfer methodology typically used to reduce these complexities is the lumped-capacity method. It provides a simplification by assuming that the interior temperature of a body is spatially uniform and varies only with time during a heat transfer process [44]. The criterion to apply the lumped-capacity method is based on a dimensionless parameter called the Biot number, Bi. In order for the lumped capacity method to be applicable to a heat transfer problem, the Biot number must be less than 0.1. The Biot number represents the ratio of conduction resistance within the body and convection resistance at the surface of the body. Therefore, a small Biot number represents a small resistance to heat conduction. Although the Biot number in this study will be less than 0.1, the heat transfer coefficient, *h*, required in the lumped capacity method is difficult to find in fire scenarios due to the mixed convection-radiation environment. Furthermore, the lumped-capacity method assumes a constant heat transfer coefficient throughout the entire heat transfer process, which does not occur in fires, and would result in large uncertainties. As a result, other transient heat conduction methodologies must be considered.

1.3.2.1 Semi-Infinite Length Models

A semi-infinite length scale model is an idealized body that has a single plane surface and extends to infinity in all directions [44]. This is advantageous because the application of the Laplace transformation removes the partial differential term that is with respect to the time variable and renders the problem

as an ordinary differential equation, where the solution can be easily obtained and is commonly referred to as the inverse heat conduction problem [45]. The complication with assuming that the material is infinite in all directions is that after long periods of exposure to heat flux, this assumption becomes invalid due to temperature changes on the backside of the material [27, 46]. In order to restrict the change in temperature of the backside, a material with low thermal conductivity is usually selected, but is undesirable for heat flux sensors as it decreases response time. Of particular interest is the work done by Fu et al. [41] where they use an inverse heat transfer method with Fourier regularization to solve the one-dimensional, heat conduction equation, referred to as the "sideways heat equation". Though this method has been shown to provide heat flux results with small errors, the numerical methods required to obtain these estimates are complex and would require complicated computer coding. However, the assumption of constant backside temperature would still fail.

1.3.2.2 Finite-length Models

To eliminate the assumption of constant backside temperature that is associated with semi-infinite models, a transient temperature boundary condition can be included on the backside of the material. This creates a finite-length scale problem where there are two planar surfaces and a finite distance between them, with both surfaces having specified boundary conditions. Therefore, if the temperature of the backside of the sensor changes, it is included in the model. This allows a highly thermally conductive material to be selected, improving the

response time of the heat flux sensor and eliminating possible temperature gradients within the medium. A powerful tool that is used extensively in literature to solve finite length scale problems are Green's functions [38, 45, 47]. This technique is useful for non-homogeneous equations. Additionally, the Laplace transformation method may also be used to solve finite length scale problems. A study conducted by Monds and McDonald [24] have shown comparisons between similar 1-D heat conduction models, revealing that use of a finite length scale model is more beneficial in measuring high heat fluxes for longer periods of time than inverse heat conduction models. Therefore, using a single analytical heat conduction solution, requiring no numerical techniques, provides greater flexibility, lower costs, and improved accuracy when compared to the semi-infinite length scale methods and finite-length scale Green's functions methods. This has led to the development of a robust, one-dimensional, finite-length scale, transient heat conduction model that was able to measure heat fluxes for extended periods of time and to eliminate the need for a constant back side temperature assumption, as in the semi-infinite models. Fundamental radiation theory is then applied to correct the results for radiation heat losses, rather than using arbitrary correction factors and constants.

1.4 Wildfire Suppression Chemicals

Various types of chemicals have been developed to aid responders in both the containment and extinguishing of wildfires. The most common chemicals act as long term fire retardants and are sprayed ahead of an advancing fire in an effort to reduce spread rate and intensity [48]. Long term fire retardants are commonly made of ammonium phosphates and coat the vegetative fuels, altering the chemical process needed for them to catch fire. Trees and brush can ignite from a stray spark, but in wildfire scenarios it occurs due to the convective and/or radiation energy applied to the tree from the moving fire front [48]. To have an unpiloted ignition, wood requires heat to induce thermal degradation of the cellulose, which is done in two processes of decomposition [49]. The first process is depolymerisation which, with enough heat, will produce volatile compounds such as alcohols, aldehydes, hydrocarbons, and ketones [49]. These escape as gases from the tree and are the cause of tree ignition. The second process is dehydration in which the cellulose breaks down into water vapor and a solid (char) which insulates the wood and prevents ignition. Fire retardants alter the balance of this decomposition in favour of the dehydration process, thus preventing ignition [49].

Although fire retardants are effective in the containment of wildfires, they are harmful to the environment. The various corrosion inhibitors and ammonia component are toxic to the environment and have a substantial impact on water quality, aquatic organisms, and land vegetation [50]. This has led to the

exploration of environmentally safe chemicals such as gels. Gels consist of a superabsorbent polymer, which absorbs 30 times its own weight of water, improving the ability of water to cling to surfaces and increases evaporation time without the detrimental environmental effects of toxic elements [7, 51]. Although gel chemicals are non-toxic, their effectiveness degrades quickly with time (two to four hours) and so they are known as short-term retardants [7]. Short-term retardants are used to extinguish the flaming and glowing phases of combustion by direct application on the burning fuel, rather than applying them ahead of a fire front [51].

To date, there has been little focus on testing the effectiveness of wildfire chemicals, other than that which has been done in manufacturer's labs. A simple specifications sheet provided by the US Forest Service has to be supplied by the manufacturer for eligibility to be listed on the Qualified Products List (QPL) [52]. Comparing the various types of suppression chemicals will aid in the strategic planning of wildfire fighting as well as reduce the immense costs necessary to contain wildfires.

1.5 Objectives

The overall objectives of this study were to:

1. Develop a simple, finite-length scale mathematical model that can estimate heat fluxes from high temperature and high heat load applications, with minimal computing requirements.
2. Fabricate a custom, low-cost, portable thermocouple-based heat flux sensor able to withstand high heat loads for extended periods of time, utilizing no external cooling.
3. Validate the performance of the sensor and model by:
    a. Testing the sensor in a controlled test environment to validate the sensor and model.
    b. Testing the sensor in a simulated forest fire environment.
    c. Comparing the heat flux results with data obtained from a Schmidt-Boelter gauge, which is a well documented and calibrated commercial sensor.

1.6 Thesis Organization

This thesis document is divided into several chapters. Chapter 2 describes the mathematical model developed to estimate heat flux. Chapter 3 describes the experimental method used to fabricate and test the novel heat flux sensor. Chapter 4 presents the results and analysis of the mathematical model, sensor data, and simulated and real fire tests. Chapter 5 presents the conclusions of this study, and Chapter 6 discusses the possible future work that may be extended from this thesis study.

2. MATHEMATICAL MODEL

2.1 Finite-length Scale Model

The heat conduction model used to determine the temperature distribution in the heat flux sensor that was exposed to the intense heat flux scenarios was based on uniform heating of a rectangular-shaped body. The analytical heat conduction model was idealized as a one-dimensional, finite-length scale problem to reduce mathematical complexity and simplify the data analysis. It was assumed that heat transfer across the exposed faces of the sensor was relatively uniform, justifying the assumption of one-dimensional heat transfer. In addition, the sides of the sensor were insulated and the high thermal diffusivity of aluminum facilitated the reduction of any thermal fluctuations that occurred.

Figure 2-1 presents a schematic for the heat transfer model. The boundary condition at the exposed face ($x = 0$ in Fig. 2-1) is one of the second kind, with the heat flux represented by $q''(t)$. The transient temperature boundary condition at the back face of the block, $x = L$, is represented by $T_1(t)$, while the internal transient temperature at $x = d$ into the block is represented by $T(d,t)$. The use of experimentally measured transient temperatures eliminated the introduction of complicated radiation and convection boundary conditions.

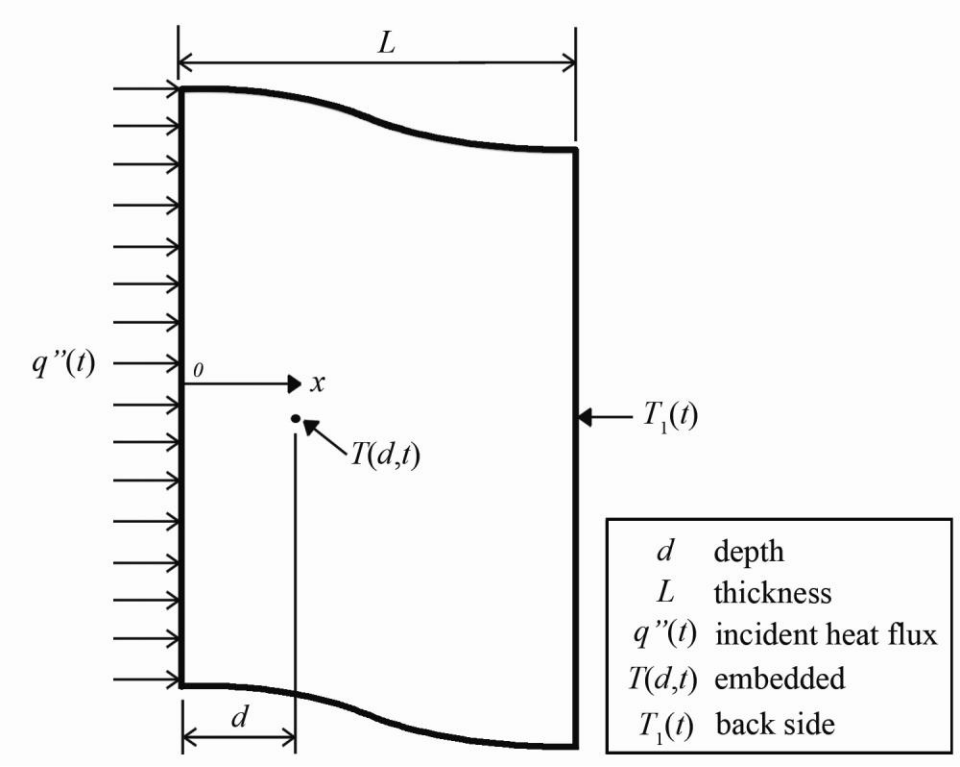

Figure 2-1: Schematic for the mathematical model

The one-dimensional governing equation for the temperature distribution in the heat flux sensor shown in Fig. 2-1 is given by

$$\frac{\partial^2 T}{\partial x^2} = \frac{1}{\alpha}\frac{\partial T}{\partial t}, \quad 0 \le x \le L, \tag{1}$$

where α is the thermal diffusivity of the material, which is defined as $\alpha = k/\rho C_p$, and represents the ability of a material to adjust to temperature changes.

The boundary and initial conditions are:

$$-k\frac{\partial T(0,t)}{\partial x}=q''(t), \tag{2}$$

$$T(L,t)=T_1(t), \tag{3}$$

$$T(x,0)=T_{\mathrm{i}}. \tag{4}$$

The boundary conditions of Eqs. (2) and (3) will render this problem non-homogeneous. Accordingly, the method of superposition and separation of variables was be used to solve the governing equation. The solution for $T(x,t)$ was assumed to be the sum of two functions, one (Ψ) depending on x and t for the homogeneous solution and the other, Φ, on x only, for the particular solution so that

$$T(x,t)=\Psi(x,t)+\Phi(x). \tag{5}$$

Substitution of Eq. (5) into Eq. (1) yields

$$\frac{\partial^2\Psi}{\partial x^2}+\frac{\partial^2\Phi}{\partial x^2}=\frac{1}{\alpha}\frac{\partial\Psi}{\partial t}. \tag{6}$$

Now separating Eq. (6) into two equations in terms of $\Psi(x,t)$ and $\Phi(x,t)$

$$\frac{\partial^2\Psi}{\partial x^2}=\frac{1}{\alpha}\frac{\partial\Psi}{\partial t}, \tag{7}$$

$$\frac{d^2\Phi}{dx^2} = 0. \tag{8}$$

The boundary conditions will also need to be transformed to accommodate the new superposition solution. Therefore, the boundary condition at $x = 0$ in Eq. (2) becomes

$$-k\frac{\partial\Psi(0,t)}{\partial x} - k\frac{\partial\Phi(0)}{\partial x} = q''(t). \tag{9}$$

To make the problem a simple homogeneous problem, it was assumed $-k\frac{\partial\Psi(0,t)}{\partial x} = 0$ and consequently, $-k\frac{\partial\Phi(0)}{\partial x} = q''(t)$. The next boundary equation at $x = L$, given in Eq. (3), then becomes

$$\Psi(L,t) - \Phi(L) = T_1(t). \tag{10}$$

Once again, to create a simple homogeneous problem, it was assumed $\Psi(L,t) = 0$ and as a result, $\Phi(L) = T_1(t)$.

Starting with the simple linear ordinary differential equation, Eq. (8) was solved by integrating, yielding

$$\Phi(x) = Ax + B. \tag{11}$$

Then substituting in boundary conditions from Eq. (9) and Eq. (10), the solution becomes

$$\Phi(x) = \frac{q''}{k}(L - x) + T_1 . \tag{12}$$

Having Eq. (8) solved, Eq. (7) was then solved. The method of separation of variables was required to solve Eq. (7). Therefore, a product solution of two functions was assumed, with *X* depending on *x* only and *τ*, on *t* only, so that

$$\Psi(x,t) = X(x)\tau(t) . \tag{13}$$

Substituting Eq. (13) into Eq. (7)

$$\frac{d^2X}{dx^2}\tau = \frac{1}{\alpha}\frac{d\tau}{dt}X \tag{14}$$

Separating the variables and setting the resulting equation equal to the separation constant $\pm\lambda_n^2$, gives

$$\frac{d^2X_n}{dx^2} \mp \lambda_n{}^2 X_n = 0 , \tag{15}$$

$$\frac{d\tau_n}{dt} \mp \alpha\lambda_n{}^2\tau_n = 0 , \tag{16}$$

Since the *x*-variable has two homogeneous conditions, the positive sign must be selected. Thus Eq. (15) and Eq. (16) become

$$\frac{d^2 X_n}{dx^2} + \lambda_n{}^2 X_n = 0, \tag{17}$$

$$\frac{d\tau_n}{dt} + \alpha\lambda_n{}^2 \tau_n = 0, \tag{18}$$

For when $n = 0$ ($\lambda_n{}^2 = 0$), the equations become

$$\frac{d^2 X_0}{dx^2} = 0, \tag{19}$$

$$\frac{d\tau_0}{dt} = 0. \tag{20}$$

Solving the ordinary differential equations by direct integration yields

$$X_0(x) = A_0 x + B_0, \tag{21}$$

$$\tau_0(t) = C_0. \tag{22}$$

Applying the boundary conditions of Eq. (9) and (10), and the initial condition, Eq. (11), the solutions for Eqs. (19) and (20) are trivial as shown by

$$\frac{d^2 X_0}{dx^2}(0) = 0 = A_0 \ \therefore A_0 = 0, \tag{23}$$

$$X_0(L) = 0 = B_0 \ \therefore B_0 = 0, \tag{24}$$

$$\tau_0(0) = 0 = C_0 \therefore C_0 = 0. \tag{25}$$

When *n* is greater than zero, the solutions to Eq. (17) and Eq. (18) are [53]:

$$X_n(x) = A_n \sin(\lambda_n x) + B_n \cos(\lambda_n x), \tag{26}$$

$$\tau_n(t) = C_n e^{-\alpha \lambda_n^2 t}. \tag{27}$$

Applying the boundary condition from Eq. (9) yields

$$\frac{\partial^2 X_n(0)}{\partial x^2} = 0 = A_n \lambda_n \cos(\lambda_n \cdot 0) - B_n \lambda_n \sin(\lambda_n \cdot 0)$$

,

$$\therefore A_n = 0$$

Applying the boundary condition from Eq. (10) gives

$$X_n(L) = 0 = B_n \lambda_n \sin(\lambda_n \cdot L),$$

Therefore, the characteristic equation for λ_n is

$$\lambda_n = \frac{(2n-1)\pi}{L} \qquad \text{for } n = 1, 2, 3\ldots, \tag{28}$$

Then, the complete homogeneous solution becomes

$$\Psi(x,t)=\sum_{n=1}^{\infty}a_n e^{-\alpha\lambda_n{}^2 t}\cos(\lambda_n x) \qquad \text{where } a_n = B_nC_n \tag{29}$$

Applying the initial condition of Eq. (4) gives

$$\Psi(x,0)=T_i=\sum_{n=1}^{\infty}a_n\cos(\lambda_n x). \tag{30}$$

To solve for a_n the concept of orthogonality was applied [53]. Equation (17) is a Sturm-Liouville equation with a weighting function, $w(x) = 1$. This was found by comparing Eq. (15) to the general Sturm-Liouville equation (see Eq. (31)) [53]:

$$\frac{d}{dx}\left[p(x)\frac{dT_n}{dx}\right]+\left[q(x)+\lambda_n{}^2 w(x)\right]T_n=0\,, \tag{31}$$

where $p(x)=e^{\int a_1 dx}, q(x)=a_2 dx, w(x)=a_3 p(x)$

For the specific case discussed, $a_1 = a_2 = 0$ and $a_3 = 1$, while $p(x) = w(x) = 1$ and $q(x) = 0$. Multiplying both sides by $\cos(\lambda_n x)dx$, integrating from $x = 0$ to $x = L$ and invoking orthogonality,

$$\int_0^L T_{\mathrm{i}}\cos(\lambda_n x)dx = a_n\int_0^L\cos^2(\lambda_n x)dx$$

$$a_n=\frac{\int_0^L T_{\mathrm{i}}\cos(\lambda_n x)dx}{\int_0^L\cos^2(\lambda_n x)dx}=\frac{T_{\mathrm{i}}\left(\dfrac{\sin(\lambda_n L)}{\lambda_n}\right)}{\dfrac{2\lambda_n L+\sin(2\lambda_n L)}{4\lambda_n}}$$

$$a_n = \frac{4T_{\mathrm{i}} \sin\left(\lambda_n L\right)}{2\lambda_n L + \sin\left(2\lambda_n L\right)} \tag{32}$$

Inserting a_n into Eq. (29),

$$\Psi\left(x,t\right) = \sum_{n=1}^{\infty} \frac{4T_{\mathrm{i}} \sin\left(\lambda_n L\right)}{2\lambda_n L + \sin\left(2\lambda_n L\right)} e^{-\alpha\lambda_n{}^2 t} \cos\left(\lambda_n x\right). \tag{33}$$

Özışık [45] solved an identical, finite-length heat conduction problem as Eq. (1), and presented the results in a table sorted by type of boundary condition, which when choosing the same homogenous boundary equations as presented, resulted in the same solution as Eq. (33).

Lastly, inserting both Eq. (12) and Eq. (33) into the superposition equation, Eq. (5), the temperature distribution in the block is [44, 53]

$$T\left(x,t\right) = \sum_{n=1}^{\infty} \frac{4T_{\mathrm{i}} \sin\left(\lambda_n L\right)}{2\lambda_n L + \sin\left(2\lambda_n L\right)} e^{-\alpha\lambda_n{}^2 t} \cos\left(\lambda_n x\right) + \frac{q''\left(t\right)}{k}\left(L - x\right) + T_1\left(t\right). \tag{34}$$

The derived equation above is a well-documented solution to a slab with a prescribed heat flux at its surface and is similar to the solutions derived by Carslaw and Jaeger [47] as well as Çengel and Ghajar [44]. The series solution of Eq. (34) decays rapidly as n and λ_n increase due to the exponential decay function [44]. Thus, for times greater than approximately two seconds, this term has negligible effect on the final solution and was neglected. The reduced solution becomes

$$T(x,t)=\frac{q''(t)}{k}(L-x)+T_1(t). \tag{35}$$

Nellis and Klein [54] found the same reduced solution as Eq. (35) by using the same governing heat conduction equation, except with two boundary conditions of the first kind to solve for the temperature distribution and then combining it with Fourier's law to obtain the heat flux. Finally, by using the transient temperature that was measured with the embedded thermocouple located at $x = d$, the expression for the unknown heat flux on the front surface of the block is

$$q''(t)=\frac{k[T(d,t)-T_1(t)]}{(L-d)}. \tag{36}$$

2.2 Estimation of Losses

2.2.1 Radiation losses

The mathematical model does not take into account the emissivity of the sensor with regards to radiation heat transfer. Therefore, Eq. (36) needs to be corrected for the radiation reflected from the surface and the radiation emitted from the sensor as it increases in temperature. The emissivity of a surface represents the ratio of the radiation emitted by the surface at a given temperature to the radiation emitted by a blackbody at the same temperature [44]. Equation (36) is the net heat flux measured at the surface of the sensor. Since the main heat transfer

mechanism in high heat flux scenarios is radiation (ignoring convection), performing an energy balance on the sensor (as shown in Figure 2-2) yields the net heat flux measured by the sensor as the incident heat flux minus the reflected and emitted heat flux to give

$$q''_{\text{net}}(t) = q''_{\text{incident}}(t) - q''_{\text{reflected}}(t) - q''_{\text{emitted}}(t). \tag{37}$$

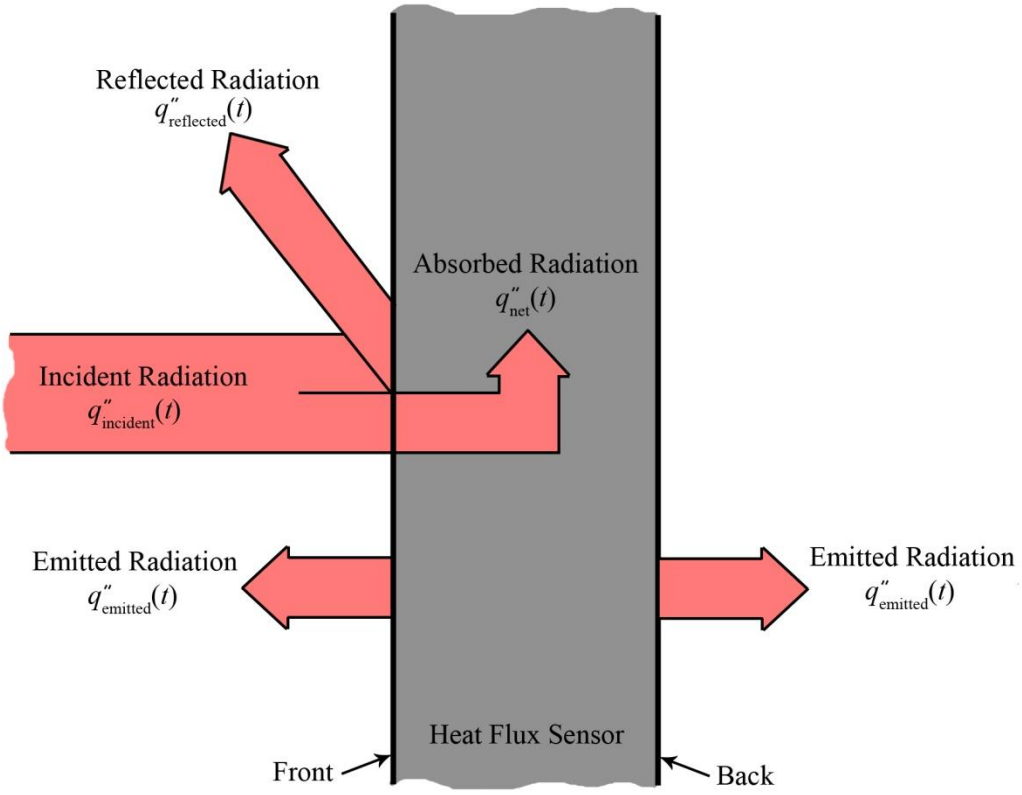

Figure 2-2: The absorption and reflection of incident radiation and emitted radiation of the heat flux sensor **[**44**]**

The reflected heat flux will depend on the absorptivity of the surface which was assumed to be equal to the emissivity. Furthermore, since the body is opaque, radiation will not transmit through the body. Therefore, the reflected heat flux is

$$q''_{\text{reflected}}(t) = (1-\varepsilon) q''_{\text{incident}} \,. \tag{38}$$

The incident heat flux was found by substituting Eq. (38) into Eq. (37) to give

$$q''_{\text{incident}}(t) = \frac{1}{\varepsilon}\left[q''_{\text{net}}(t) + q''_{\text{emitted}}(t)\right]. \tag{39}$$

The sensor that was developed in this study was not water-cooled. Therefore, the temperature of the sensor developed in this study will increase over the duration of the test. This will result in radiation heat loss from the heat flux sensor to the ambient surroundings from both the back side and front side of the sensor since the back side was also open to the ambient surroundings. To compensate for the emitted radiation heat loss, the Stefan-Boltzmann law [44] was included in the model,

$$q''_{\text{emitted}}(t) = \sigma\varepsilon\left(T(x,t)^4 - T_\infty^4\right). \tag{40}$$

The incident heat flux on the surface of the sensor then becomes

$$q''_{\text{incident}}(t) = \frac{1}{\varepsilon}\left(\frac{k\left[T(d,t) - T_1(t)\right]}{(L-d)} + \sigma\varepsilon\left[T(d,t)^4 + T_1(t)^4 - 2T_\infty^4\right]\right). \tag{41}$$

Similar radiation theory and heat conduction techniques were used by Häggkvist et al. [36] resulting in a comparable equation to Eq. (41) except Häggkvist et al. [36] only measured one temperature and used correction factors which introduced

significant error for the low values of time (less than 4 mins) and did not include reflected radiation.

2.2.2 Convective heat losses

To investigate the effects of natural convection in a mixed radiation-convection environment, which is common in a forest fire, the Rayleigh number, Ra, was examined:

$$\mathrm{Ra}_H = \frac{g\beta(T_s - T_\infty)H^3 \,\mathrm{Pr}}{\upsilon^2}, \tag{42}$$

where g is gravity, β is the compressibility factor of the fluid, $(T_s - T_\infty)$ is the temperature difference between the surface of the sensor and the ambient surroundings, H is the height of the sensor, Pr is the Prandtl number, and υ is the kinematic viscosity of the fluid. The Rayleigh number is a non-dimensional parameter that is associated with buoyancy-driven flow. It confirms the possibility of free convective currents at the front face of the sensor, further increasing the energy loss due to convection [44, 55]. To obtain a first order estimate of the heat loss due to convection, the temperature difference between the surface of the sensor and the ambient surroundings was assumed to be 600 K. The assumption of a 600 K temperature difference was based on the measured air temperatures from field experiments conducted by other investigators [26, 56]. Although the sensor will never reach the air temperature measured by these researchers, it will

be an indication of the maximum convective losses at the maximum temperature the sensor can experience before reaching the melting point of the sensor (933 K). The properties of air were found from Çengel and Ghajar [44] at the film temperature $\left(T_f = \frac{(T_s - T_\infty)}{2} = 300 \text{ K} \right)$, and are shown in Table 2-1. The resulting Rayleigh number was calculated to be 4.6 x 10^5, which is well below the critical Rayleigh number (10^9) for transition from laminar to turbulent free convective flow [55]. It is also an indication that turbulent natural convective flow will not occur over the sensor since the surface temperature of the sensor that would be required to create this condition was beyond the melting point of the sensor material.

Table 2-1: Properties of air at film temperature [44]

Temperature (K)	k (W-m^{-1}-K^{-1})	Pr	υ (m^2 s^{-1})	β (K^{-1})
50	0.02735	0.7228	1.798x10^{-5}	2x10^{-2}
300	0.04418	0.6935	4.765x10^{-5}	3.33 x10^{-3}

It was assumed that the exposed surfaces of the sensor experienced laminar free convection, which can be modelled as flow over a vertical plate subjected to uniform surface heat flux. The average convective heat transfer coefficient was calculated using the similarity solution given by Jiji [55]. The average heat transfer coefficient, $\bar{h}$, was calculated to be 13.3 W-m^{-2}-K^{-1}. With Newton's law of cooling [55],

$$q_s'' = \bar{h}(T_s - T_\infty), \tag{43}$$

the estimated heat flux lost due to free convection from the surface of the sensor was 8 kW-m^{-2}. Since there are two sides of the sensor exposed to ambient, the total heat flux lost due to free convection would be 16 kW-m^{-2}. Although these convective losses are significant when the sensor is at its maximum temperature, in a forest fire setting, air temperature would not remain constant. Consequently, as the surface temperature of the sensor approaches thermal equilibrium with the air temperature, the temperature difference decreases, resulting in less convective losses.

To provide a more realistic temperature difference the sensor will endure, a 100 K temperature difference was assumed and the corresponding air properties shown in Table 2-1. The estimated total heat flux lost due to free convection from both surfaces of the sensor was calculated to be 1.7 kW-m^{-2}. This estimate of the free convective losses that occur proves to be negligible compared to the intense heat fluxes measured during forest fires, which are on the order of 20 – 80 kW-m^{-2} [56]. It would be difficult to incorporate the convective heat transfer losses into Eq. (41) since it would require iterations, complex coding, and the measurement of air properties during tests. This would further complicate data analysis and would require additional instrumentation.

3. EXPERIMENTAL METHOD

The primary purpose of the experimental work performed in this study was to provide heat flux data from simulated and real fires in order to validate the finite-length scale mathematical model and test the performance of the custom-fabricated thermocouple-based heat flux sensor. To accomplish this, constant heat flux, simulated fire tests and a surface fire test were conducted using a mass loss cone calorimeter (Mass Loss Calorimeter ISO 13927, Fire Testing Technology, East Grinstead, West Sussex, UK), a radiant panel (MYAC Consulting, Sherwood Park, AB, Canada), and a grass field plot, respectively.

3.1 Sensor Construction

The custom-made heat flux sensor, hereinafter referred to as the "thermal cube", was a 50.8 mm x 63.5 mm x 25.4 mm (2 in x 2.5 in x 1 in) rectangular block of 6063-T6 aluminum, with three thermocouples inserted for temperature measurement (See Appendix A for engineered drawing). The front and back side of the block was painted with a high-temperature black spray paint (Krylon 1618 BBQ and Stove Paint, The Sherwin-Williams Company, Cleveland, OH, USA) to increase the emissivity so that it approached that of an ideal black-body and to enhance absorption of almost all radiation heat transfer. Three 1.98 mm (0.078 in) holes were drilled into the aluminum block to allow for insertion of the thermocouples, as shown in Fig. 3-1. The thermocouples were installed in the holes, which corresponded to locations at x = 3.2 mm, x = 12.7 mm, and

x = 22.2 mm. The thermocouple that was located in the middle of the slab provided temperature data that was used to validate the mathematical model of Eq. (36) by predicting the transient temperature after the heat flux value was estimated. The data from the thermocouples was used to generate transient temperature profiles and to establish the boundary condition of Eq. (3).

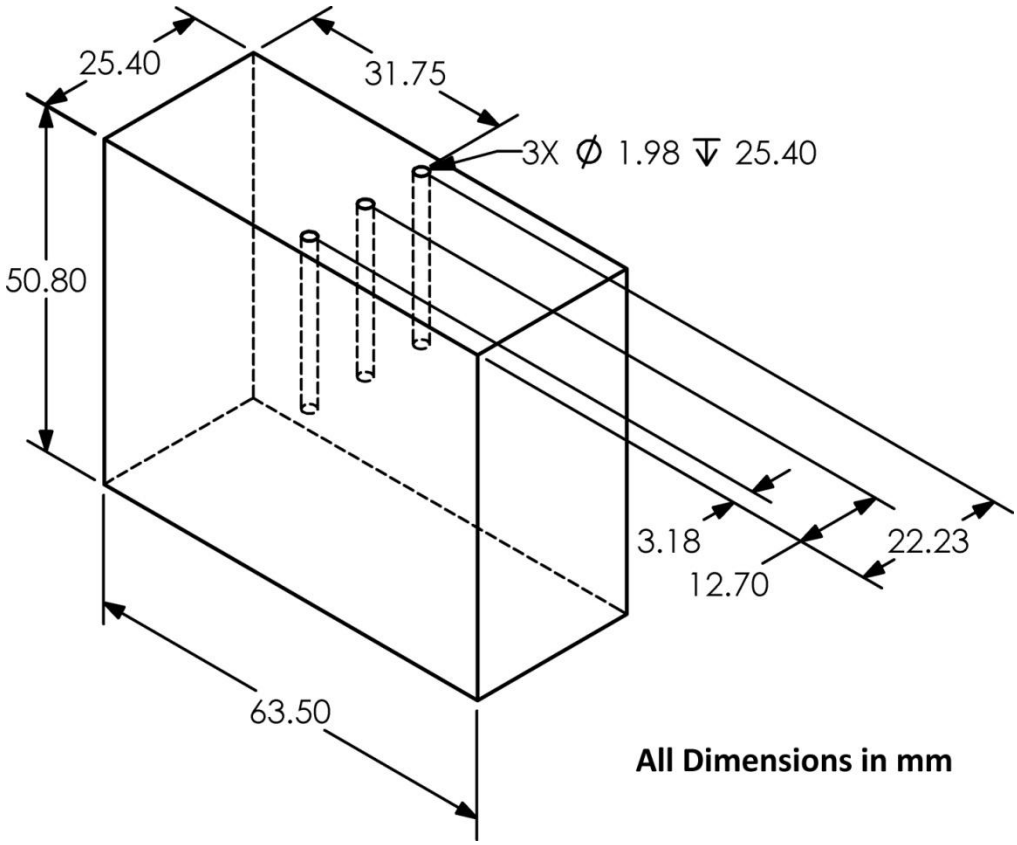

Figure 3-1: Dimensions of the thermal cube (All dimensions in mm)

Type-J, 30 gauge thermocouples (iron-constantan) (Omega Engineering, Inc., Laval, QC, Canada) were selected due to their ability to measure temperatures over a broad temperature range (-210 to 750°C), high sensitivity

(51 μV-ºC^{-1}), and low cost. No special glue or adhesive was applied to enhance the contact between the thermocouple because the hole was sufficiently small enough to provide a tight interference fit. The thermal conductivity of the 6063-T6 aluminum that was used in this study was 200 W-m^{-1}-°C^{-1} [57]. Aluminum was chosen because of its high thermal conductivity, high melting point of approximately 580 to 650ºC [58], and relatively constant thermal conductivity at elevated temperatures beyond 0^{o}C [59]. The sides of the thermal cube were then insulated using M-board insulation (M-board, Industrial Insulation Group, Augusta, GA, USA) in order to drive one-dimensional transfer of energy through the cube (see Fig. 3-2). In addition, the high thermal conductivity of the aluminum also aided to justify the one-dimensional assumption by reducing edge effects.

To establish a benchmark for the tests and to provide data for comparison, a Schmidt-Boelter gauge (64 series, Medtherm Corporation, Huntsville, AL, USA) was installed in the M-board insulation as shown in Fig. 3-2. A Schmidt-Boelter gauge was selected since it can measure both total heat flux and radiative heat flux. Given that in this study, the thermal cube will measure the total heat flux from the heat source, only the data of the total heat flux obtained from the commercial gauge was used. The cooling water flow rate for the Schmidt-Boelter gauge was set to approximately 30 L-hr^{-1}, with the water at approximately 25ºC.

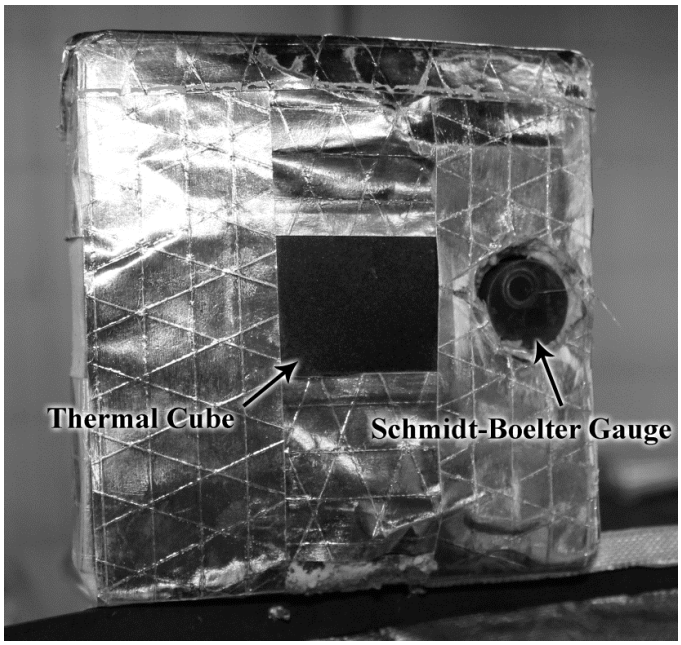

Figure 3-2: Assembly of thermal cube and Schmidt-Boelter gauge in M-board insulation

3.2 Mass Loss Cone Calorimeter Validation Tests

Validation tests were conducted with a constant heat flux by way of a mass loss cone calorimeter (Mass Loss Calorimeter ISO 13927, Fire Testing Technology, East Grinstead, West Sussex, UK). By adjusting the temperature of the element in the mass loss cone calorimeter, heat fluxes of up to 100 kW-m^{-2} were generated. For this test, the temperature of the element was set to 550ºC to generate a heat flux of approximately 50 kW-m^{-2}. This heat flux was selected due to the heat fluxes observed in the field by Butler et al. [26] and Silvani and Morandini [56]. The sensors were positioned horizontally at 2.5 cm (1 in) from the edge of the mass loss cone calorimeter as shown in Fig. 3-3.

Figure 3-3: Mass loss cone calorimeter test apparatus

The heat flux was varied by opening a shutter for two minutes, closing for one minute, and then reopening for another two minutes to evaluate the response of the sensor and prove that the sensor was capable of measuring large, abrupt changes of heat flux. Each test was preformed twice to ensure repeatability and the sensor was cooled to within ±10°C of the first test to ensure the sensor was starting at a similar point. In addition, an extended heat flux measurement test was conducted where the shutter was left open for 10 minutes to evaluate the effectiveness of the sensor when exposed to long periods of intense heat flux.

For each test, the results were collected using a stand-alone data acquisition and analysis system (DaqPRO^{TM} 5300, Fourier Systems Inc., Mokena, IL, USA). The data acquisition system used a 16-bit system with 8 channels for data collection. The temperature measurements were collected at a sampling rate of 1 Hz for all the thermocouples, as well as voltage measurements from the Schmidt-Boelter gauge.

3.3 Oxy-acetylene Flame Spray Torch Test

Flame tests were conducted using a thermal spraying oxy-acetylene flame spray torch (6PII ThemoSpray Gun, Sulzer Metco Inc., Westbury, NY) mounted on a robot (HP-20, Motoman, Yaskawa Electric Corp., Waukegan, IL, USA) to test the thermal cube's ability to measure heat flux when subjected to direct flame contact. The thermal cube was mounted to the substrate holder using C-clamps and the thermocouples attached to the DaqPRO logger. Figure 3-4 shows the test apparatus when the torch was positioned at the centered of the cube.

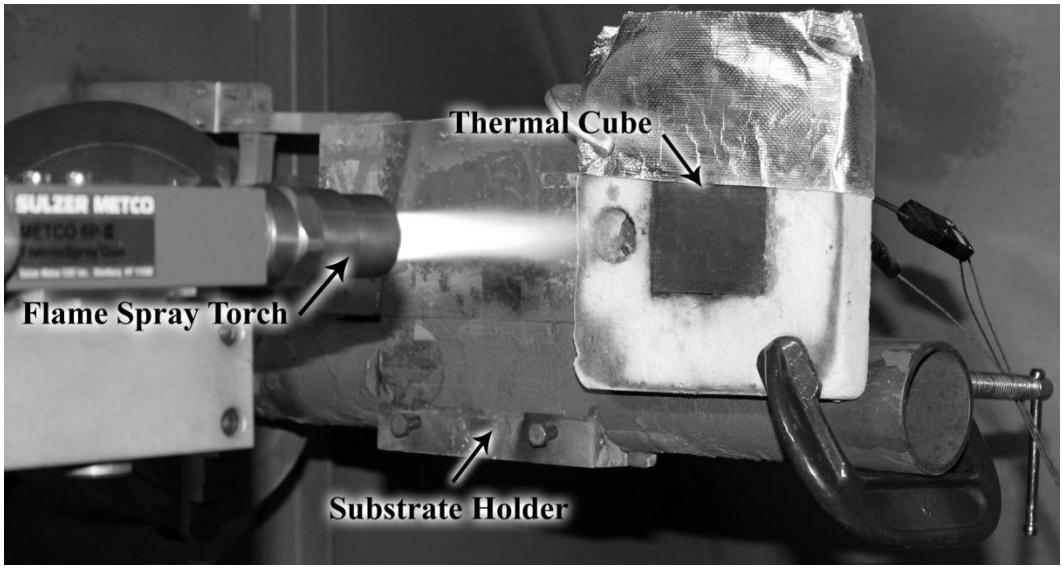

Figure 3-4: Oxy-acetylene flame spray torch test setup

In order to generate the flame, 6 normal liters per minute (NLM) of acetylene and 15 NLM of oxygen were combusted together using the flame spray torch, where the pressures of acetylene and oxygen were 103 kPa (15 psig) and 241 kPa (35 psig), respectively. The robot was first programmed to have a stand-off distance (distance between the sensor surface and the torch) of 21.5 mm from the center of the thermal cube and held in that position for 30 seconds, as shown in Fig. 3-5 as P1. The torch was then moved away for 10 seconds to allow the thermal cube to measure the subsequent drop in heat flux. Next, the torch was moved back to the cube at the same stand-off distance, but at 25.4 mm (1 in) below the center of the cube for a period of 30 seconds, denoted as P2 in Fig. 3-5. This process was repeated twice at distances of 50.8 mm (2 in) and 63.5 mm (2.5 in) below the center of the cube, shown in Fig. 3-5 as P3 and P4, respectively. Three additional tests were conducted to ensure repeatability and accuracy.

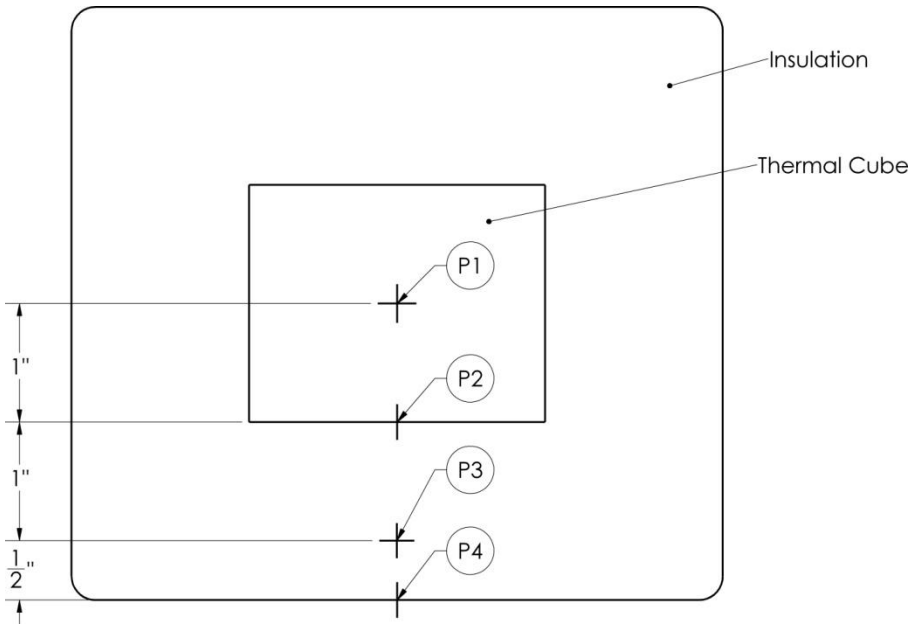

Figure 3-5: Positions of center of torch along the thermal cube during the oxy-acetylene flame spray torch tests

3.4 Surface Fire Field Test

To test the model in a practical field environment, a grass fire burn test was conducted in Chisholm, Alberta where transient temperature data was collected. The grass section was divided into plots approximately 12 m x 50 m long using fire breaks provided by Alberta Sustainable Resource Development (ASRD). Two plots were burned with different vegetation types. One being reed grass (Calamafrastis) and the other a mixture of plateaus fescue, white clover, yarrow, and Agronomix (Alberta Innovates, Vegreville, Canada). The goal of these planted plots was to show that the mixed vegetation had a slower, less intense fire when compared to the reed grass.

The sensor was placed in the ground, mounted on a pole approximately 3 m from the ignition line with a small hole dug below the sensor approximately 30 cm deep in order to bury an 8-channel logger, as shown in Fig. 3-6a. This served to protect the logger from the fire. The three thermocouples in the sensor were then attached to the first three channels of the logger and were set to take a sample every second (1 Hz sampling rate). The logger was wrapped in plastic bags to protect the logger from water and placed in the hole beneath the sensor. The hole was then covered with dirt. Both sensors were placed at similar distances from the ignition line for comparative purposes. The grass was then ignited using a drip torch, as shown in Fig. 3-6b, and was burned to completion.

(a) (b)

Figure 3-6: Surface grass fire: (a) sensor and logger placement and (b) ignition of reed grass using a drip torch

3.5 Simulated Tree Fire Tests

3.5.1 Radiant panel testing apparatus

Simulated forest fire tests with a radiant panel (MYAC Consulting, Sherwood Park, Alberta, Canada) were used in this study. The radiant panel was used to simulate similar heat fluxes that would be present in real forest fire situations. The radiant panel assembly is shown in Fig. 3-7. The assembly included the panel, a trolley that was used to adjust the distance between the panel by using an electric motor, a tree holder, and the sensors. The radiant panel consisted of seven propane gas-fired infrared burners (EcoSchwank 26, Schwank, Waynesboro, GA, USA), each having an input of 29.3 kW (100,000 Btu-hr^{-1}) for a total input of 205.2 kW (700,000 Btu-hr^{-1}). By stacking the burners on top of each other, the radiant panel had dimensions of 1.12 m wide by 1.16 m tall (44 in by 45.5 in). The trolley was made to roll along the frame using an electric motor, potentiometer, and chain. By measuring the voltage of the potentiometer, the location of the trolley was determined and, therefore, set to the same position throughout all the tests. The assembly was adjusted by varying the distance of the trolley in order to vary the heat flux on the sensor up to 50 kW-m^{-2}.

A 1.25 m tall by 0.64 m (49 in x 22 in) diameter lodgepole pine was placed in the holder on the trolley as shown in Fig. 3-7. The sensors were placed behind the tree at a height of 1 m (40 in) above the trolley. The panel was switched on and allowed to heat up for one minute. The trolley was moved into position where the trunk of the tree was 0.33 m (13 in) and sensors were 66 cm

(26 in) from the panel. The tree was then subjected to the heat flux produced by the panel and burned to completion, as shown in the image of Fig, 3-8.

Figure 3-7: Experimental assembly for simulated fire tests

Figure 3-8: Tree burning in the radiant panel assembly

4. RESULTS AND DISCUSSION

4.1 Constant Heat Flux

4.1.1 Cone calorimeter step tests

The resulting transient temperatures and heat fluxes that were estimated from the thermal cube data and model for one of the representative tests conducted with the mass loss cone calorimeter are shown in Fig. 4-1. The temperature profiles shown in Fig. 4-1a are linear and show the temperature difference between the front and back side of the sensor. Even though the temperature difference is small, the model is able to predict the heat flux that was measured experimentally. It also shows that the sensor is capable of measuring heat fluxes at elevated temperatures, where the sensor reached a maximum temperature of 247°C.

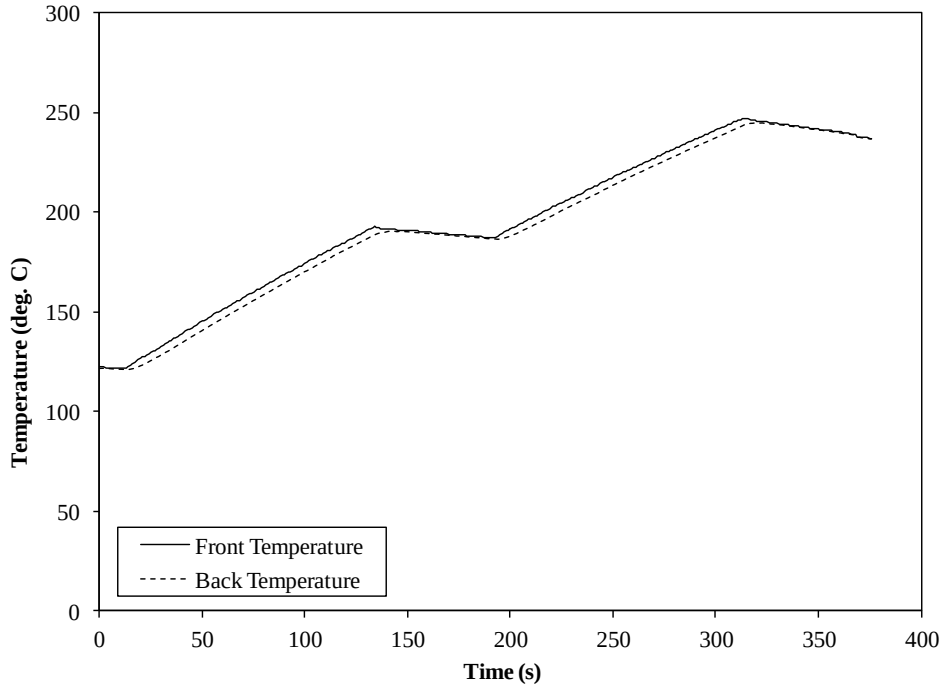

(a)

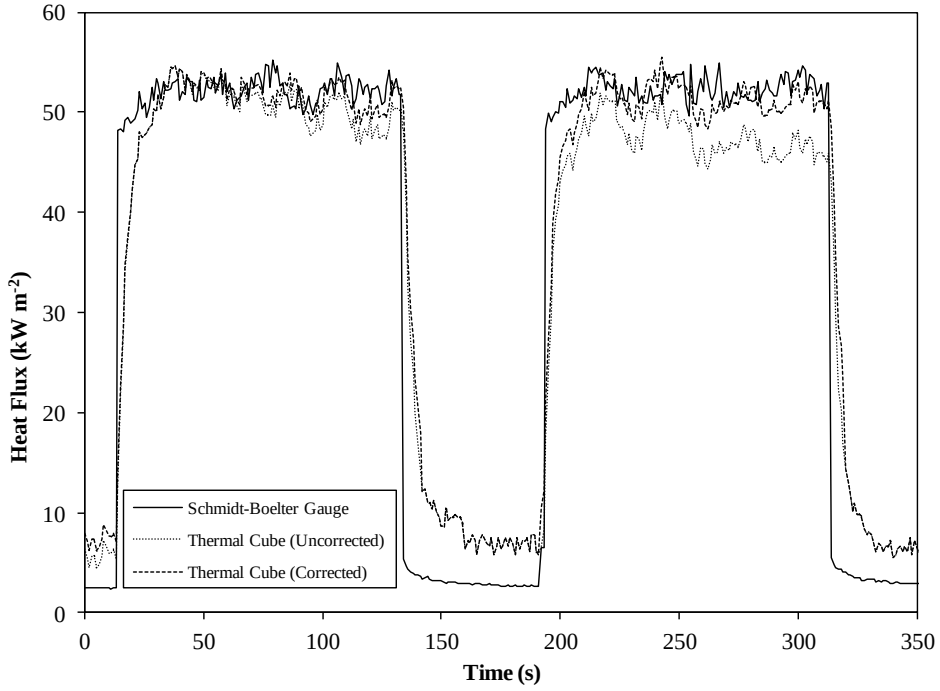

(b)

Figure 4-1: Curves from tests with the mass loss cone calorimeter showing (a) transient temperatures and (b) transient incident heat fluxes

Figure 4-1b shows close agreement between the measured heat flux values of the commercial Schmidt-Boelter gauge and those measured by the thermal cube. Equation (41) was used to generate data points for the transient incident heat flux curve, as predicted with temperature data from the thermal cube. It can be seen that as the measured temperature of the thermal cube increases, there is an increase in deviation between the measured and calculated incident heat flux values. Figure 4-1b also shows a transient heat flux curve for data that was generated from Eq. (36) for the thermal cube, where re-radiation and reflected radiation were not considered. It is clear from the figure that the deviation between the reported transient heat flux from the uncorrected thermal cube and the Schmidt-Boelter gauge is larger than the case when radiation and emissivity are considered in the problem. At the start of the test and data collection, a small time delay of approximately eight seconds was recorded between the heat flux prediction of the thermal cube and the measured heat flux of the Schmidt-Boelter gauge. This is likely due to resistance induced by inserting the thermocouple within the aluminum block at a depth of 3.18 mm (0.125 in). At the end of the tests (approximately 140 and 310 s in Fig. 4-1b), the heat flux decreases suddenly as the source of heat flux is removed. The observed discrepancy in the heat flux between that predicted by the thermal cube and that measured by the Schmidt-Boelter gauge at the end of the test is due to the emitted radiation from the thermal cube to the shutter of the mass loss cone calorimeter and ultimate reflection back to the thermal cube. This also occurred with the Schmidt-Boelter gauge as it measured a small heat flux at the end of the test (see Fig. 4-1b).

However, due to its smaller surface area, the measured heat flux was lower than that which was estimated by the thermal cube.

The target heat flux from the mass loss cone calorimeter was 50 kW-m^{-2}. From Fig. 4-1b, it is observed that, at steady state, the heat flux values fluctuate slightly. This level of noise is likely due to turbulence in the air flow caused by a fan within the mass loss cone calorimeter and the small clearance between the edge of the calorimeter and the sensors. This induced some turbulent convective heat transfer, which produced small variations in the steady state heat fluxes on the order of approximately 1 - 2 kW-m^{-2}. The average steady state heat flux that was measured using the Schmidt-Boelter gauge over all three tests was 52 ± 1 kW-m^{-2} (n = 676), while for the thermal cube, it was 52 ± 3 kW-m^{-2} (n = 676). The standard deviation is provided with the averages. These average steady state heat flux values confirm that the results obtained from the thermal cube are in good agreement with those measured experimentally by the established commercial sensor. The values predicted by the thermal cube, coupled with the mathematical model of Eq. (41), were within one standard deviation of those obtained from the commercial Schmidt-Boelter gauge.

4.1.2 Cone calorimeter test

In industrial practice, the measurement and/or estimation of heat fluxes from high heat load sources such as wildland fires will need to be captured over long time periods. Figure 4-2 shows heat flux results from both the thermal cube

and the Schmidt-Boelter gauge for extended operation of the mass loss cone calorimeter. The thermal cube slightly over-predicted the heat flux at the beginning of the test, eventually coming into good agreement with those obtained from the Schmidt-Boelter gauge. The decreasing trend with the thermal cube is due to the rising temperature of the aluminum, which causes an increase of convective losses and is the reason that there is an approximately 3 kW-m^{-2} variation from the start of the test until the end of the test. Similar observations have been recorded for non-cooled gauges such as the DFT and HFG sensors as seen in the work done by Lam and Weckman [32]. The average heat fluxes measured from an extended period of operation were 54 ± 2 kW-m^{-2} (n = 595) and 56 ± 2 kW-m^{-2} (n = 595) for the Schmidt-Boelter gauge and the thermal cube, respectively. Although, a decreasing trend is occurring, the average heat flux was still within one standard deviation of the commercial gauge. Furthermore, the thermal cube was able to measure intense heat fluxes over extended time periods similar to those seen in field experiments. Silvani and Morandini [56] have shown that heat fluxes of burning vegetative fuels ranges from 20 to 80 kW-m^{-2}, for periods of three to four minutes. This suggests that the thermal cube would perform satisfactorily under conditions of outdoor field fires, given that the experimental tests whose results are presented in Fig. 4-2 were conducted for approximately 10 minutes. Heat fluxes that were measured by the thermal cube correlate to the maximum heat flux to which a given surface would be exposed in a fire scenario. Radiation and convective effects are highly dependent on surface and material properties and, therefore, materials such as bark, fuel particles, or

soil would likely absorb an incident heat flux that is lower than the gross total energy released in a fire scenario. Methods to relate these heat fluxes to other materials of interest would need to be investigated in future work and is discussed in a study by Bova and Dickinson [43].

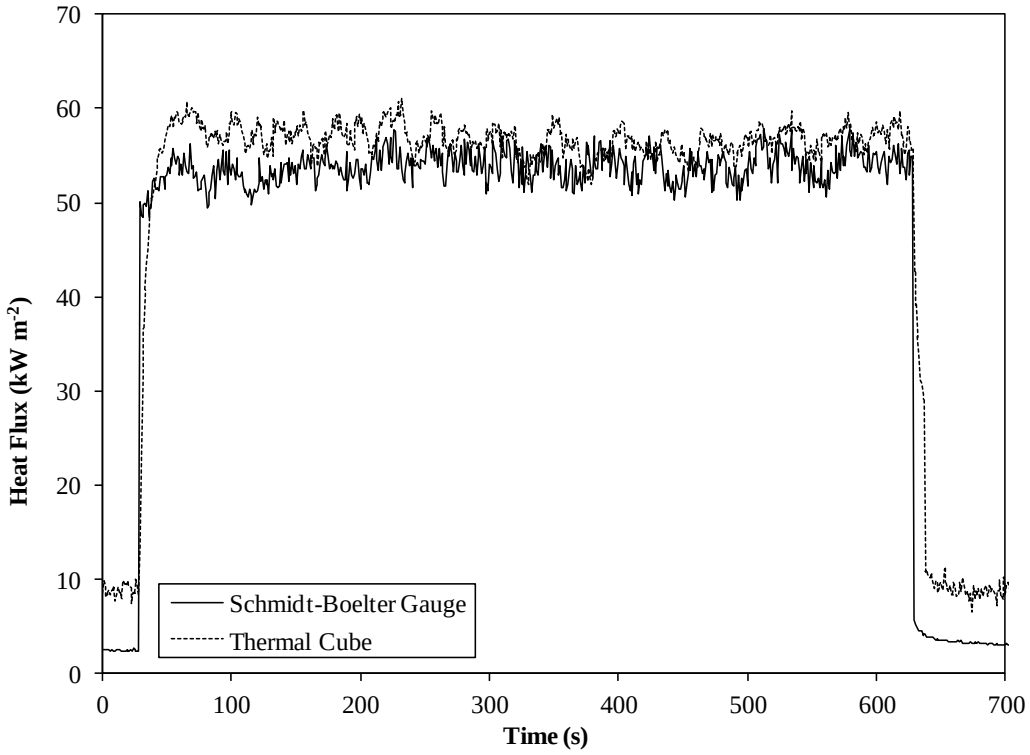

Figure 4-2: Curves of transient incident heat flux from a mass loss cone calorimeter over an extended test period

4.1.3 Oxy-acetylene flame spray torch tests

The resulting heat fluxes that were estimated from the model with thermal data from the thermal cube data and the oxy-acetylene flame spray torch are shown in Fig. 4-3. The four oxy-acetylene flame spray torch positions can be clearly seen in the heat flux peaks. The first peak represents the location of the

torch at the center position (P1), the second peak at 25.4 mm (1 in) below the center (P2), and so forth. The test is then repeated two more times as can be seen be the repeating pattern of heat flux spikes. The resulting average heat fluxes for each peak in each test are shown in Table 4-1. The average heat fluxes over all three tests for the positions P1, P2, P3, and P4 (as shown in Fig. 3-5) along the sensor are: 46 ± 3 kW-m^{-2} (n = 67), 38 ± 2 kW-m^{-2} (n = 67), 23 ± 2 kW-m^{-2} (n = 81), and 17 ± 1 kW-m^{-2} (n = 83), respectively.

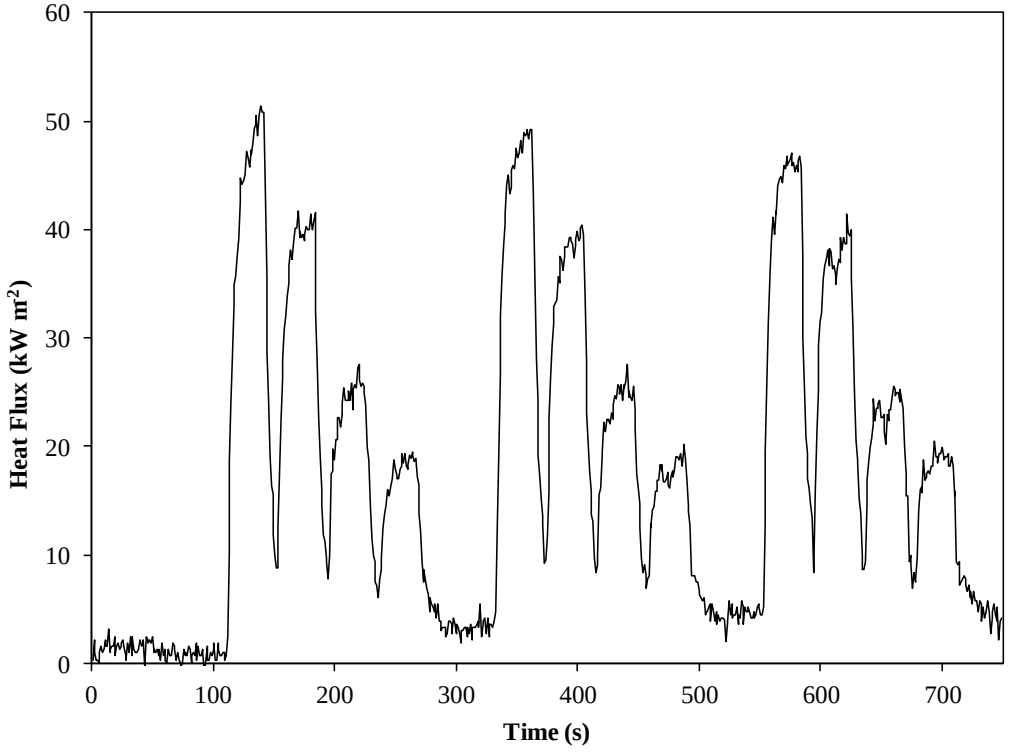

Figure 4-3: Transient incident heat flux curves from oxy-acetylene flame test

The thermal cube performed well in all three tests, showing that the tests are highly repeatable when using the thermal cube for heat flux measurements.

The heat flux measured does decrease as the tests progress due to increasing convective heat transfer to the ambient surroundings on the exposed surfaces of the thermal cube as well as re-radiation from the thermal cube, similar to the mass loss cone calorimeter tests. The reflected radiation and re-radiation losses have been considered, but it is difficult to estimate convective losses due to the surface temperature dependence of the free convection heat transfer coefficient, as well as its dependence on surface orientation, air speed, fluid properties, to name a few. However, a first order estimate of the losses have been shown in Section 2.2.2, where the free convection losses were found to be on the order of 1.7 kW-m^{-2} when the temperature of the sensor was at 120°C. In Test 3 of the flame spray torch test (Table 4-1), the sensor reached a maximum temperature of 142°C and it was estimated that the heat flux was 3 kW-m^{-2} less than that of Test 1, which confirms the presence of free convective losses and is comparable to the losses estimated in Section 2.2.2. Despite these loses, the thermal cube still predicted heat fluxes that were in close agreement with experimental data, with small standard deviations over all three tests. This suggests that the thermal cube is capable of measuring heat flux from direct flame contact.

Table 4-1: Heat flux data from the oxy-acetylene flame spray torch tests

	Test 1			**Test 2**			**Test 3**		
Position	**Mean**	**Std. Dev.**	***n***	**Mean**	**Std. Dev.**	***n***	**Mean**	**Std. Dev.**	***n***
Center (P1)	48	2	20	47	2	23	45	2	24
1 in below (P2)	40	1	21	38	1	22	38	2	24
2 in below (P3)	25	2	25	24	2	27	23	2	29
2.5 in below (P4)	18	1	28	18	1	27	18	1	28

4.1.4 Performance comparison of the thermal cube sensor

The performance of the thermal cube was compared to that of a commercial Schmidt-Boelter gauge, and the outcome is shown in Table 4-2. The thermal cube has a similar working range, but a lower response time than the Schmidt-Boelter gauge. The working range of the thermal cube is specified as up to 65 kW-m^{-2}, given that it was only tested up to that heat flux but further investigation into its limits are suggested in future work. The emissivity of the two systems are assumed to be similar as well as their fields of view. The most significant difference is the cost of the systems and the requirement for external cooling of the commercially available gauge. The thermal cube requires no water cooling and because of its simple construction, it has lower cost.

Table 4-2: Specifications of heat flux sensors

	Thermal Cube	**Schmidt-Boelter Gauge** [60]
Working Range (kW-m^{-2}):	10 to 65	5, 10, 20, 50, 100, 200
Response Time:	8 seconds @ 50 kW m^{-2}	< 450 ms for 5, 10 kW-m^{-2} range
		< 250 ms for 20, 50 kW-m^{-2} range
		< 200 ms for 100, 200 kW-m^{-2} range
Emissivity:	~ 0.95	> 0.95
Field of view:	180 degrees	180 degrees
Cooling water temperature:	N/A	10 - 30°C
Cooling water flow:	N/A	> 10 L/hr
Approximate cost:	$50 CAD	$1200 - $3200 CAD [61, 62]

The thermal cube is constructed of a single material, instead of a composite of materials like that of the Directional Flame Thermometer (DFT) in the work of Keltner, et al. [29]. The materials used in the DFT sensor have a

temperature-dependent thermal conductivity which makes the governing heat conduction equation non-linear. Therefore, using a simple, homogeneous material with a constant thermal conductivity in the range of temperatures of interest creates a linear problem and further simplifies the analysis. Given all the features listed, the thermal cube allows fire scientists to purchase more sensors, place multiple heat flux sensors in various locations, and expand their data collection capabilities.

The simple, linear mathematical model for the thermal cube has been used to calculate heat fluxes without the use of complicated computer programming. When compared to the models developed by Monds and McDonald [24], who also used a transient temperature boundary condition, their Green's function analysis required iterations due to the summation within the Green's function, while the model proposed in this study has no summation. The thermal cube was also able to estimate heat fluxes for greater periods of time than both the semi-infinite and finite-length scale models used by Monds and McDonald [24]. This was due to the use of a transient temperature and heat flux boundary condition in this study, rather than two transient temperature boundary conditions as was done by Monds and McDonald [24]. Furthermore, Peridier [63] used the same heat conduction equation of Eq. (1), but used a cellular automaton energy-transport method to solve for the unknown heat flux, thus, requiring computer programming and advanced mathematics. The proposed model in this study requires no advanced mathematics or computer programming to obtain the desired

heat flux and will estimate reasonable values of the total heat flux from various high heat load scenarios.

4.2 Surface Fires

4.2.1 Reed grass

Reed grass was ignited and was quick to become a fast moving fire. The outdoor conditions were measured using a pocket weather meter (Kestrel 2500, Nielsen-Kellerman, Boothwyn, PA, USA). The ambient environment temperature was 10 - 12°C with a relative humidity (RH) of 55% and a wind speed of 5 - 10 km/h in the direction of the fire. The rate of spread of the fire was approximately 10 m/min, which was measured using a stop watch and two meter-long sticks placed in the ground every 5 meters perpendicular to the ignition line. The transient heat flux calculated from the model as measured by the sensor is shown in Fig. 4-4.

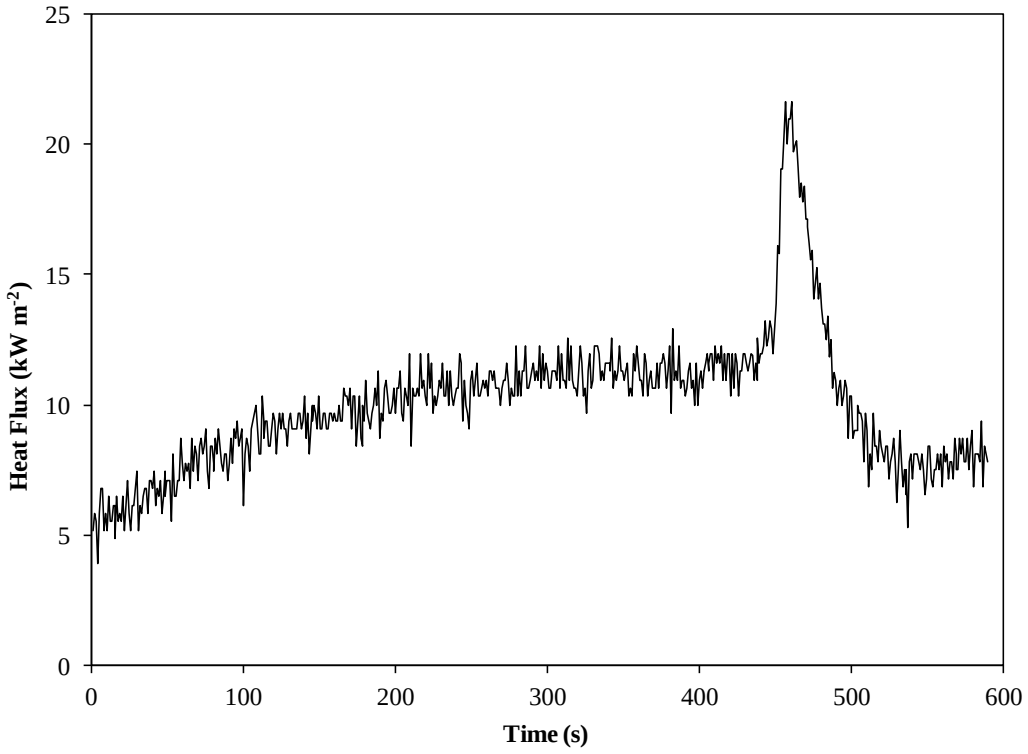

Figure 4-4: Transient incident heat flux curve from reed grass surface fire

The heat flux does not begin at zero due to the logger being started as the fire was approaching the sensor. The heat flux then slowly increased as the fire approached and then a sharp spike occurs as the flame engulfs the sensor completely and continues burning past it. The thermal cube observed a max heat flux of 22 kW-m^{-2} and then decreased quickly as the fire passed the sensor. Silvani and Morandini [56] observed similar heat flux results in their pine needles and oak branches tests, having large heat flux spikes as well. After the fire had passed, a small amount of energy remained due to some small spot fires that were still burning.

4.2.2 Vegetation mixture

The mixed vegetation plot was ignited with an even stronger wind of 10 - 15 km/h and the same temperature and RH as the reed grass test. However, the rate of spread of the fire was lower than that of the reed grass and was not measured because the fire would not travel far enough to take a measurement before it self-extinguished. The fire moved very slowly and had a visibly less intense flame front due to its reduced flame height and dark flame color [64]. The heat flux calculated from the sensor and model are shown in Fig. 4-5. The heat flux slowly increases as the fire front moves towards the sensor. The rate of spread was very slow as can be seen by the small slope of the heat flux in the figure. The peak heat flux observed in the mixed vegetation plot was 9 kW-m^{-2}, which was 12 kW-m^{-2} less than that in the burning reed grass. There appears to be more noise in the transient heat flux curve for the mixed vegetation test. This is likely due to the increased wind speed, which increased the heat convection transfer to the sensor. Also, the smaller scale of the *y*-axis of Fig. 4-5 will give the appearance of higher noise levels in the data. Additionally, a small temperature difference, which occurs below 10 kW-m^{-2}, will result in a large amount of error and is thus also a contributor to the high level of noise. This is discussed further in the Future Work section of this thesis. The use of the thermal cube sensor showed that the mixed vegetation was successful in decreasing the rate of spread as well as fire intensity when compared to reed grass.

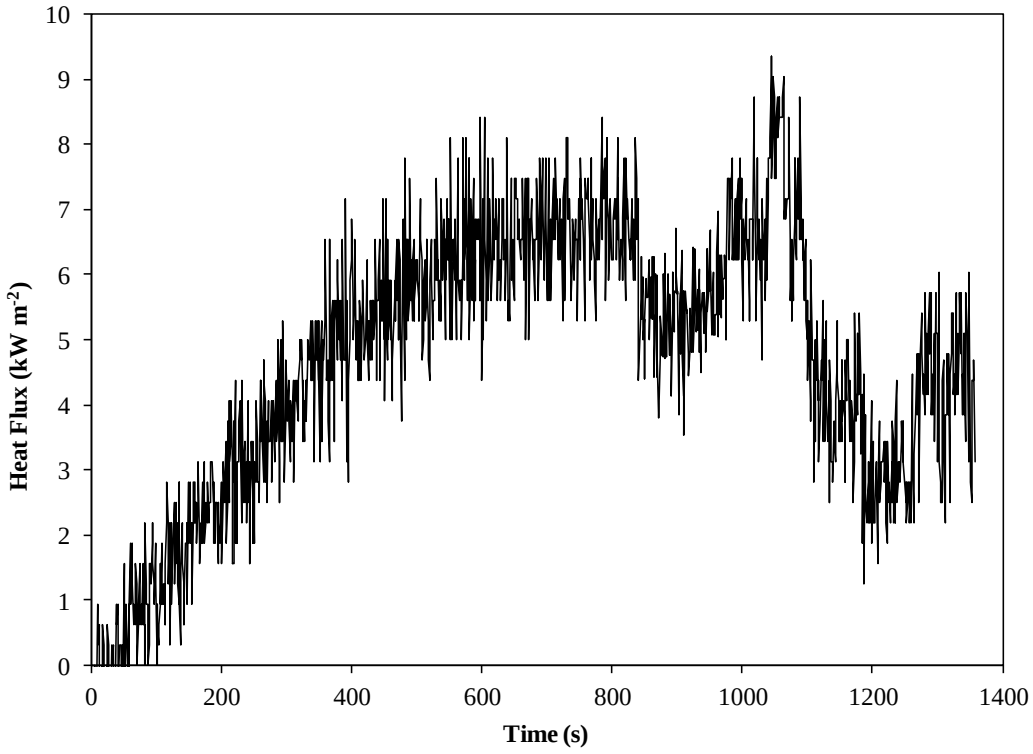

Figure 4-5: Transient incident heat flux curve from mixed vegetation surface fire

4.3 Tree Burning

Simulated fire tests were conducted with lodgepole pine tree samples from Fort Providence, Northwest Territories, Canada to further assess the performance of the new thermal cube. The resulting heat fluxes that were estimated during the simulated fire test are presented in Fig. 4-6. At t = 11 s, the panel was set in operation and allowed to heat up as indicated by the small rise in heat flux between t = 11 s and 85 s. At t = 85 s, the trolley was moved to a position that was 0.10 m away from the panel. At that point, there was a significant increase in the heat flux from 4 to 12 kW-m^{-2}. The heat flux remained approximately constant

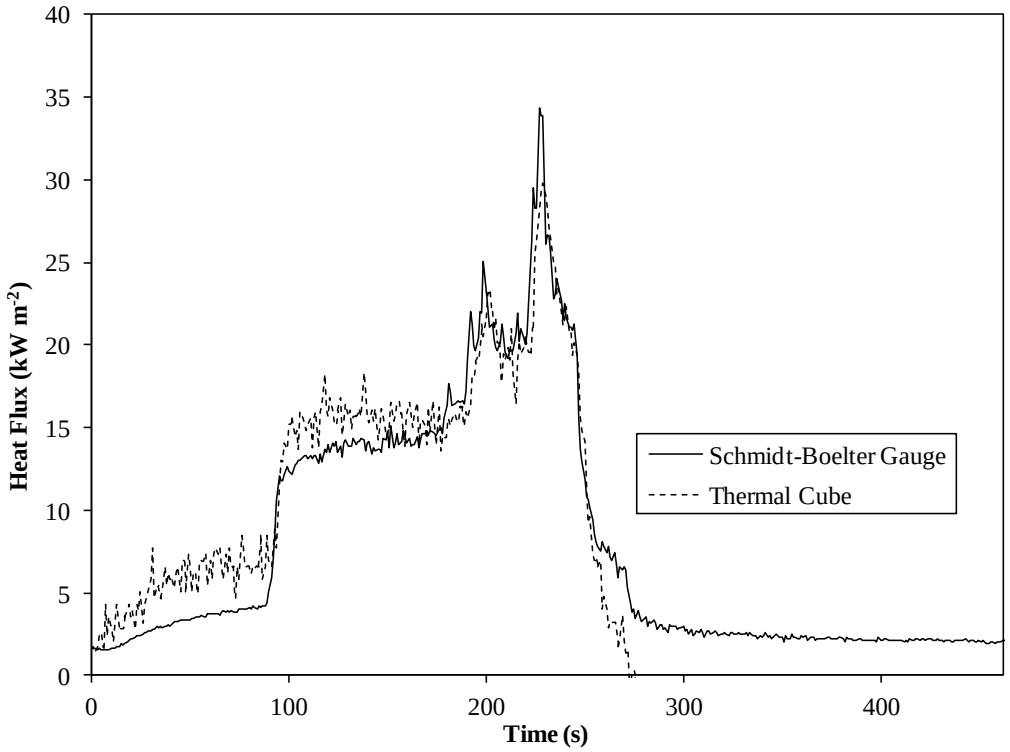

Figure 4-6: Curves of transient incident heat flux from a burning tree

until t = 180 s into the test. At that time, the tree ignited into flames, and this event is indicated by the rapid, fluctuating increase in the heat flux. Silvani and Morandini [56] observed similar trends in the heat flux profiles in their field experiments, indicating that the thermal cube performs in a similar fashion to that observed by others during measurement of heat fluxes from burning vegetative fuels. The tree burned for approximately 65 s, with a peak heat flux of 34 kW-m^{-2} (see Fig. 4-6). The sudden, singular decrease in the heat flux at t = 245 s indicates that the radiant panel was no longer operational and that the tree had burned to completion. The heat flux data that was estimated from the thermal cube shows a negative heat flux because the aluminum block was re-radiating energy back to the panel and the environment from the front side of the sensor at a rate that was

faster than that from the backside. The results presented in Fig. 4-6 suggest that in addition to estimating the total heat flux from burning vegetative fuel in a simulated fire scenario, the novel thermal cube heat flux sensor and model can be used to identify ignition of the fuel and calculate time-to-ignition.

4.4 Time to Ignition of Vegetative Fuels

The results of this study were applied to the investigation of the ignition time of vegetative fuels coated with three common fire suppressant chemicals, namely gel, fire retardant, and water. The thermal cube sensor, along with the Schmidt-Boelter gauge, was positioned at the same location as in the simulated tree burning tests. The trees used in the tests were the same as the radiant panel exposure tests, lodgepole pine which had been dried for two weeks prior to testing. The suppressant chemicals were applied using an apparatus provided by the United States Forest Service (USFS) which consisted of a pipe enclosure to hold a tarp, a manifold with two 45° nozzles, a compressed air chemical tank, a ball valve, and a rotating base. The tree was then placed on a rotating base in the tarpaulin enclosure and clamped to the base using three bolts to pinch the trunk of the tree. The wildfire chemical was then mixed according to manufacturer's specifications. The chemicals tested were a gel chemical (Thermo-Gel, Thermo Technologies, Bismarck, ND, USA) and a fire retardant (Phos-Chek LC-95A, ICL Performance Products, Kamloops, BC, Canada). The fire retardant was mixed to the manufacturer's specification of 5.5 volume parts of water per volume of

concentrate (See Appendix B for specifications) as well as 11 volume parts of water per volume of concentrate to test the effectiveness of a normal mixture and a thinned mixture. The chemical mixture was prepared using a paint mixer attached to a cordless drill for approximately 5 minutes. The mixture was poured into a tank, sealed with a lid, and filled with compressed air to a pressure of 345 kPa (50 psi). The base was turned on and allowed to rotate using an electric motor and chain assembly where the base rotated at 4 RPM. The ball valve was then opened to allow the chemical to flow through the nozzles for two full rotations of the base, which was approximately 30 seconds to coat the tree. Next, the tree was removed from the application apparatus and moved to the radiant panel apparatus where the tree was placed in a holder to prevent it from falling forward. The tree was then subjected to the heat flux of the radiant panel and heat flux data was recorded using both the sensors.

From the heat flux data collected from the tests, the ignition time can be calculated based on the sharp increases in the heat flux as shown in Fig. 4-7 (Point D) for the heating and burning of an untreated tree. Similar interpretations of signals have been studied by McDonald et al. [65], where a relation between the patterns of voltage signals indicated the occurrence of a physical phenomenon or a change in a measured parameter such as in this study, where large heat flux singularities indicate the events shown in Fig. 4-7. The heat flux sensor was used to provide qualitative indication of ignition and initiation of flames that cause burning of vegetative fuels. Other investigators [66] have used custom-fabricated sensor technology to qualify observed phenomenon. The area denoted as A (Fig.

4-7) represents the initiation of the burners of the panel and that were allowed to warm up. The trolley was moved into position as seen in the heat flux increase in the area denoted by B. The ignition time is the area denoted by C since this is the area where the tree is subjected to radiant heat flux from the panel before it ignites. The point D is the time at which the tree first ignites as indicated by the observed spike in heat flux which corresponds to the generation of a flame. Lastly, the tree then continues to burn as is seen in the area denoted by E, with the more intense heat flux and large spikes due to the flames.

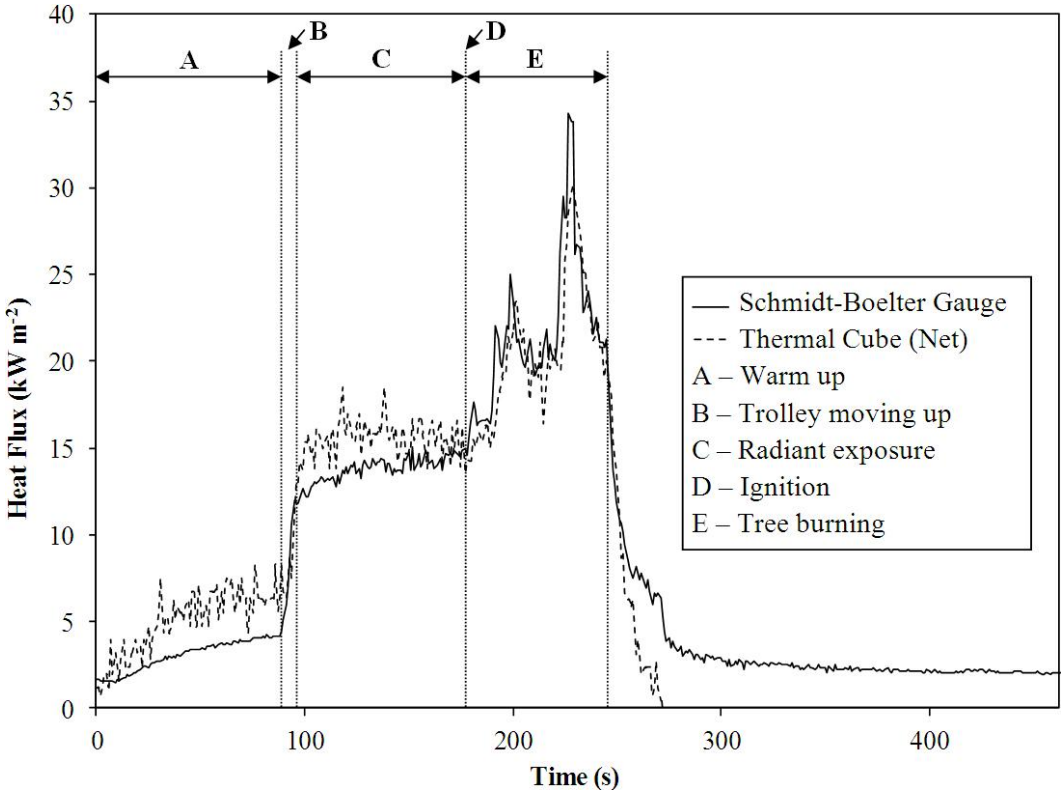

Figure 4-7: Interpretation of heat flux data to calculate ignition time

The water-treated trees allowed some of the radiant heat energy to be used to transform the liquid water into vapor, thus increasing the ignition time. Unfortunately, water does not adhere to the needles or branches for long periods of time [51], but is the least expensive option in wildfire suppression. Therefore, gel chemicals were developed to increase the viscosity of the water to adhere to the needles and branches of the tree more effectively. Similar to water, the radiant heat energy in the beginning of the test was consumed by the evaporation of the water within the gel, causing an increase in the ignition time. This can be observed in the results shown in Table 4-3 [51].

Table 4-3: Comparison of ignition times for wildfire chemicals

Treatment	**Time to Ignition Average from Thermal Cube (s)**	**Time to Ignition Average from Ault et al. (s)** [67]
Untreated	45 ± 2 (n = 2)	38 ± 4
Water	67 ± 5 (n = 2)	62 ± 21
Gel	114 ± 27 (n = 3)	87 ± 37
Retardant, dry (5.5:1)	80 ± 3 (n = 2)	67 ± 24
Retardant, wet (5.5:1)	Did not burn	Did not burn
Retardant, wet (11:1)	129 ± 2 (n = 2)	74 ± 46

For the untreated trees, water, gel, and thinned retardants, after the trees had burnt to completion, none of the needles remained. This left only the trunk and some remnants of the branches as shown in Fig. 4-8a. In the cases of the manufacturer-specified mixture strength (5.5:1) retardant, after the trees had burnt to completion, the needles remained on the trees and were charred by the radiant exposure as shown in Fig. 4-8b. This clearly identified the ability of the retardant to shift the balance of the decomposition process to the dehydration side as

discussed in section 1.4. This dehydration prohibited the breakdown of the cellulose and consequently, prevented the release of volatile organic compounds (VOCs) that are easily ignitable.

(a) (b)

Figure 4-8: Comparison of trees after burning (a) untreated with its needles all burnt and some remnant branches and (b) treated with wet (5.5:1) long-term retardant having most of its needles and branches still intact

The best performing wildfire suppression chemical was the wet, long-term retardant which did not burn even after 7 minutes of exposure. The thinned retardant and gel performed similarly by almost doubling the time to ignition. Water and dried retardant were the least effective in delaying ignition time. The average ignition times of the suppression chemicals that were tested and that were measured by the thermal cube are shown in Table 4-3. The results of ignition time that were estimated through use of the thermal cube sensor are compared with measurements gathered by Ault et al. [67] for the same vegetative fuels and treatment conditions. The thermal cube sensor measured ignition times that were all longer than those observed by Ault et al. [67]. Ault et al. [67] measured the ignition times by observing the heating of the fuels and noting the time when the ignition occurred by visual observation. Visual time was recorded at the sight of the first flame, which occurred at the bottom branch that was closest to the panel where the incident heat flux was large. The heat flux from this flame was shielded by the structure of the tree and therefore produced a time delay until the tree flames became large enough to be observed by the sensors at the back of the trolley, which were approximately 76 cm (30 in) from the point of ignition. The largest difference occurred with the wet, 11:1 retardant due to the slow flame propagation. This caused a significant delay due to the poor positioning of the sensors at the back of the trolley resulting in the sensors not being able to measure the heat flux until the flames were large enough. These results suggest that measuring heat flux with the developed thermal cube sensor can be an effective

method to calculate the ignition time of trees when testing wildfire chemicals if the sensors are positioned closer to the initial source of ignition.

4.5 Error Analysis

An uncertainty analysis was conducted on Eq. (41) to determine the amount of error that can occur due to the accuracy of the instrumentation and devices. The issue of uncertainty occurred during investigation of surface fire tests (Section 4.2), in which high noise levels in the heat flux data were observed. There are eight variables, ε, k, σ, T_∞, $T(d,t)$, $T_1(t)$, L, and d in Eq. (41), which may have uncertainty that affects the accuracy of the heat flux estimate. Beginning with the emissivity, ε, and thermal conductivity, k, the associated error was assumed to be zero even though in practice they would have an error. These values were either assumed or not measured and acquired from other researchers. Using the same argument, the ambient temperature will also have zero error as it was an assumed value that was taken to be constant. The Stefan-Boltzmann constant is also assumed to have an error of zero because it is a well-known and documented constant in the Stefan-Boltzmann law. For the temperature measurements, $T(d,t)$ and $T_1(t)$, these variables were measured using Type-J thermocouples in which the manufacturer provides the associated error as 1.1°C [68]. Lastly, the error associated with the position of the thermocouples, L and d, was determined by the accuracy of the measuring tape used to mark the center of

the holes, and the error in the measurement was 1 mm. This is common practice as shown by Taylor [69]. The error for each variable is tabulated in Table 4-4.

Table 4-4: Uncertainties of variables in Eq. (41)

Variable	ε	k	σ	T_∞ (°C)	$T(d,t)$ (°C)	$T_1(t)$ (°C)	L (in)	d (in)
Error	0	0	0	0	1.1	1.1	0.0394	0.0394

To calculate the propagation of uncertainty, the equations derived from Taylor [69],

$$\omega_q = \sqrt{\left(\omega_{x_1}\right)^2 + ... + \left(\omega_{x_n}\right)^2} \quad \text{for} \quad q = x_1 + ... + x_n , \tag{44}$$

$$\frac{\omega_q}{|q|} = \sqrt{\left(\frac{\omega_{x_1}}{x_1}\right)^2 + ... + \left(\frac{\omega_u}{u}\right)^2 + \left(\frac{\omega_{x_n}}{x_n}\right)^2} \quad \text{for} \quad q = \frac{x_1 \cdot ... \cdot x_n}{u}, \tag{45}$$

$$\frac{\omega_q}{|q|} = |n|\frac{\omega_x}{|x|} \quad \text{for} \quad q = x^n , \tag{46}$$

were used to evaluate the propagated uncertainty in the heat flux estimations. By using Eqs. (44), (45), and (46), and applying them to Eq. (41), the propagated uncertainty in the estimated heat flux is

$$\left(\frac{\omega_{q''_{net}}}{q''_{net}}\right)^2 = \left(\frac{\left[\left(\omega_{T_1(t)}\right)^2 + \left(\omega_{T(d,t)}\right)^2\right]^{1/2}}{T_1(t) - T(d,t)}\right)^2 + \left(\frac{\left[\left(\omega_L\right)^2 + \left(\omega_d\right)^2\right]^{1/2}}{(L-d)}\right)^2 + 8\left(\frac{\omega_{T_1(t)}}{T_1(t)}\right)^2 + 8\left(\frac{\omega_{T(d,t)}}{T(d,t)}\right)^2 . \tag{47}$$

Values from the mass loss cone calorimeter test, one at a high heat flux of 64.2 kW-m^{-2} and one at a low heat flux of 12.7 kW-m^{-2} (shown in Table 4-5) were used in Eq. (47) to calculate errors of 32 % and 143%, respectively.

Table 4-5: Sample values from mass loss cone calorimeter test for error calculation

Test:	High heat flux (64.2 kW-m^{-2})	Low heat flux (12.7 kW-m^{-2})
t (s)	67	29
$T(d,t)$ (°C)	125.25	99.83
$T_1(t)$ (°C)	120.08	98.74
L (in)	0.875	0.875
d (in)	0.125	0.125
T_∞ (°C)	22	22
Calculated Error:	32%	143%

Both of these errors are unacceptable in common engineering practice. The largest error was a result of the thermocouple errors of 1.1°C for each temperature measurement. This poses a serious problem when measuring the small temperature difference that occurs within the sensor and must be addressed in future work. Some recommendations to decrease this error, is to manufacture a composite sensor to decrease the thermal conductivity in the middle portion of the sensor and thus increase the temperature difference and improve accuracy. Another option would be to use a single material, but choose one with a lower conductivity, which would also increase the temperature difference. However, this would reduce the response time, which may be of importance in wildfire applications where heat loads have durations on the order of two to five minutes. Increasing the thickness of the block would also prove to be a viable option. A

final option to improve accuracy would be to measure the temperature difference directly by wiring the thermocouples to read only a temperature difference rather than two individual temperatures.

5. CONCLUSIONS

The primary objective of this study was to develop a robust heat conduction model based on a finite-length scale that was coupled with an inexpensive custom-fabricated sensor that would be capable of measuring intense heat fluxes in forest fire scenarios without the use of external cooling. The model and sensor would be able to measure high heat fluxes for extended periods of time, where sensors utilizing semi-infinite mathematical models would not apply. Furthermore, a practical application of the thermal cube was investigated by evaluating various wildfire suppression chemicals where wet fire retardant, mixed at the manufacturer's specifications of 5.5:1, delayed the ignition time of the vegetative fuel the longest when compared to water, gel, dried retardant and thinned retardant treatments.

The mathematical model that was developed has been shown to be capable of estimating the total heat flux from both a constant heat flux source and a simulated forest fire scenario, all within one standard deviation of the values measured by a commercial Schmidt-Boelter heat flux gauge. The sensor was also able to withstand direct flame contact in the oxy-acetylene torch tests and surface fire tests. The model was simplified to a simple linear equation, requiring no special computer programming in order to calculate the estimated heat flux. From the tests conducted, the sensor performed well in both controlled laboratory tests and simulated forest fire tests. The thermal cube sensor was able to measure high heat fluxes for extended periods of time without the use of external cooling. As a

result, this durable sensor was inexpensive in comparison to commercial heat flux gauges. This will allow fire scientists to place multiple heat flux sensors in various locations and expand their data collection capabilities.

From the practical application of the thermal cube, the investigation of suppression chemicals tested yielded useful results on the effectiveness of these various chemicals. To date, there is no standard for testing these suppression chemicals and therefore, experimental results on the efficacy of treatments are needed. Applying water, thinned retardant, or dried normal strength retardant was successful in approximately doubling the time to ignition when compared to the untreated trees. Thermo-Gel was able to delay the ignition time by 2.5 times that of an untreated tree. Normal strength (5.5:1) retardant applied "wet" was capable of completely preventing ignition, even after 7 minutes of intense heat flux exposure. This was due to ammonium phosphates altering the balance of the decomposition process of the cellulose in the wood to favor the dehydration process.

From this thesis study, it has been shown that it is possible to measure intense forest fire heat fluxes using a simple, low cost, thermocouple-based aluminum sensor requiring no water cooling and using a simple linear mathematical model to estimate heat flux.

6. FUTURE WORK AND RECOMMENDATIONS

Further work is required to separate the radiation and convective components of the total heat flux that was measured. This would involve the construction of a more complex sensor that would be similar to the Schmidt-Boelter gauge or the introduction of more complicated boundary conditions in the mathematical model to isolate the convective and radiative components. In addition, an optimization of the thermal cube may also be done to reduce the size of the sensor further and to make it more portable and versatile. Methods to relate the heat flux measurements to a material of interest such as trees, fuel particles and soil could also be further investigated to expand the versatility of the heat flux data collected. Finally, the thermal cube would need to be calibrated according to ISO 14934 [70], which is a standard for the calibration and use of heat flux meters for fire tests, to allow for final commercial use.

To decrease the error by the thermocouple measurements, a composite sensor could be manufactured to decrease the thermal conductivity in the central portion of the sensor and thus increase the temperature difference, improving accuracy. Another option would be to continue use of one material, but choose one with a lower conductivity, which would also increase the temperature difference. However, response time would be reduced. Insulating the backside of the sensor would also reduce losses occurring at the back of the sensor and eliminate the need to estimate convective and radiation losses occurring at the backside. The accuracy of the sensor may also be improved by measuring the

temperature difference directly by wiring the thermocouples to read only a temperature difference rather than two individual temperatures.

In the evaluation of suppression chemicals, several factors such as moisture content, the structure of the trees, type of trees, and position in the radiant panel assembly had a significant impact on the ignition times. Therefore, using real trees is not the ideal method of evaluating ignition times. Some improvements could be made using a constant structure and/or using a material with consistent moisture content. Additionally, the position of the thermal cube to measure the heat flux was essential in calculating the ignition time. To refine the ignition time results, positioning the sensor closer to the area of suspected ignition would reduce the deviation in results from the visual ignition times. Further investigation into using a finite-length model and thermocouple based sensor to estimate fuel consumption, rather than ignition time, could be explored to improve comparisons between various suppression chemicals.

7. References

[1] R. C. Balling, G. A. Meyer and S. G. Wells, "Relation of surface climate and burned area in Yellowstone National Park," *Agricultural and Forest Meteorology*, vol. 60, no. 3-4, pp. 285-293, 1992.

[2] E. K. Heyerdahl, L. B. Brubaker and J. K. Agee, "Annual and decadal climate forcing of historical fire regimes in the interior Pacific Northwest, USA," *Holocene,* vol. 12, no. 5, pp. 597-604, 2002.

[3] A. L. Westerling, H. G. Hidalgo, D. R. Cayan and T. W. Swetnam, "Warming and Earlier Spring Increase Western U.S. Forest Wildfire Activity," *Science,* vol. 313, no. 5789, pp. 940-943, 18 August 2006.

[4] M. Chas-Amil, J. Touza and E. Garcia-Martinez, "Forest fires in the wildland-urban interface: A spatial analysis of forest fragmentation and human impacts," *Applied Geography*, vol. 43, pp. 127-137, 2013.

[5] OIG (Office of the Inspector General), "Audit report: Forest Service large fire suppression costs," San Francisco, USDA Office of the Inspector General Western Region: Report No 08601-44-SF, 2006, p. 4.

[6] D. Gavin, D. Hallett, F. Hu, K. Lertzman, S. Pichard, K. Brown, J. Lynch, P. Bartlein and D. Peterson, "Forest fire and climate change in western North America: insights from sediment charcoal recoards," *Frontiers in Ecology and the Environment,* vol. 5, pp. 449-506, 2007.

[7] K. Alvarez and E. Gomez, Forest fires: detection, suppression and prevention, New York: Nova Science Publishers, 2009, p. 288.

[8] British Columbia Forest Service, "Fire Review Summary for Okanagan Mountain Fire (K50628)," British Columbia Ministry of Forests, 2003, pp. 1-11.

[9] ESRD (Environment and Sustainable Resource Development), "Final report from the Flat Top Complex Wildfire Review Committee," Edmonton, Alberta ESRD, 2012, pp. 1-95.

[10] P. N. Omi, Forest Fires, Santa Barbara: ABC-CLIO, 2005, p. 102.

[11] W. W. Knorr, T. T. Kaminski, A. A. Arneth and U. U. Weber, "Impact of human population density on fire frequency at the global scale," *Biogeosciences Discussions,* vol. 10, no. 10, pp. 15735-15778, 2013.

[12] S. J. Pyne, P. L. Andrews and R. D. Laven, Introduction to wildland fire, New York: Wiley, 1996, p. 66.

[13] A. Alvarez, M. Gracia, J. Vayreda and J. Retana, "Patterns of fuel types and crown fire potential in Pinus halepensis forests in the Western Mediterranean Basin," *Forest Ecology And Management,* vol. 270, pp. 282-290, 2012.

[14] J. Barrows, "Fire behaviour in Northern Rocky Mountain forests," Missoula, USDA Forest Service Station Pap. 29, 1951, pp. 1-120.

[15] R. Kremens, A. Smith and M. Dickinson, "Fire Metrology: Current and Future Directions in Physics-Based Measurements," *Fire Ecology,* vol. 6, no. 1, pp. 13-35, 2010.

[16] G. M. Bryam, "Combustion of forest fuels," in *Forest Fire Control and Use*, New York, NY: McGraw-Hill, 1959, pp. 61-89.

[17] F. Morandini, Y. Perez-Ramirez, V. S. P. Tihay and T. Barboni, "Radiant, convective and heat release characterization of vegetation fire," *International Journal Of Thermal Sciences,* vol. 70, pp. 83-91, 2013.

[18] J. E. Keeley, "Fire intensity, fire severity and burn severity: a brief review," *International Journal of Wildland Fire,* vol. 18, pp. 116-126, 2009.

[19] R. M. Nelson and C. W. Adkins, "Flame characteristics of wind-driven surface fires," *Canadian Journal Of Forest Research,* vol. 16, no. 6, pp. 1293-1300, 1986.

[20] S. W. Taylor, M. E. Alexander and R. G. Pike, Field guide to the Canadian Forest Fire Behavior Prediction (FBP) System, Victoria: Canadian Forest Service, 1996, pp. 9-33.

[21] Steel Construction Institute (SCI), "Heat Flux Loading," in *Use of Ultimate Strength Techniques for Fire Resistant Design of Offshore Structures: (FABIG Technical Note 3)*, Silwood Park, Steel Construction Institute (SCI), 1995, pp. 11-13.

[22] E. M. Sparrow and R. C. Cess, Radiation Heat Transfer - Augmented ed., Washington, D.C.: Hemisphere, 1978.

[23] C. J. Wieczorek and N. A. Dembsey, "Human Variability Correction Factors for Use with Simplified Engineering Tools for Predicting Pain and Second Degree Burns," *Journal Of Fire Protection Engineering,* vol. 11, no. 2, p. 88, 2001.

[24] J. Monds and A. McDonald, "Determination of skin temperature distribution and heat flux during simulated fires using Green's functions over finite-length scales," *Appl. Thermal Eng.,* vol. 50, pp. 593-603, 2013.

[25] D. Frankman, B. Webb, B. Butler, D. Jimenez, J. Forthofer, P. Sopko, K. Shannon, J. Hiers and R. Ottmar, "Measurements of convective and radiative heating in wildland fires," *International Journal Of Wildland Fire,* vol. 22, no. 2, pp. 157-167, 2013.

[26] B. W. Butler, J. J. Cohen, D. J. Latham, R. D. Schuette, P. P. Sopko, K. S. Shannon, D. Jimenez and L. S. Bradshaw, "Measurements of radiant emissive power and temperatures in crown fires," *Canadian Journal Of Forest Research,* vol. 34, no. 8, pp. 1577-1587, 2004.

[27] R. M. Anguiano, "Transient Heat Transfer through Thin Fibrous Layers," Edmonton, University of Alberta, MSc. Thesis, 2006, p. 93.

[28] J. M. Cavanagh, "Clothing Flammability and Skin Burn Injury in Normal and Micro-Gravity," Saskatoon, University of Saskatchewan, MSc. Thesis, 2004, p. 14.

[29] N. R. Keltner, J. V. Beck and J. T. Nakos, "Using Directional Flame Thermometers for Measuring Thermal Exposure," *Journal of ASTM International,* vol. 7, no. 2, pp. 27-43, 2010.

[30] M. A. Sultan, "Performance of Different Temperature Sensors in Standard Fire Resistance Test Furnaces," *Fire Technology,* vol. 46, no. 4, pp. 853-881, 2010.

[31] C. S. Lam and E. J. Weckman, "Heat Flux Measurements and Their Uncertainty in a Large-Scale Fire Test," *Journal Of Testing & Evaluation,* vol. 39, no. 6, pp. 1049-1059, 2011.

[32] C. Lam and E. Weckman, "Steady-state heat flux measurements in radiative and mixed radiative-convective environments," *Fire And Materials,* vol. 33, no. 7, pp. 303-321, 2009.

[33] M. Samuel L., P. Seul-Hyun and C. Thomas G., "Development of rapidly deployable instrumentation packages for data acquisition in wildland–urban interface (WUI) fires," *Fire Safety Journal,* vol. 45, no. 5, pp. 327-336, 2010.

[34] S. S. Sudheer, L. Kumar, B. S. Manjunath, A. Pasi, G. G. Meenakshi and S. V. Prabhu, "Fire safety distances for open pool fires," *Infrared Physics & Technology*, vol. 61, pp. 265-273, 2013.

[35] M. Svantner, P. Vacikova and M. Honner, "IR thermography heat flux measurement in fire safety applications," *Infrared Physics & Technology*, vol. 55, no. 4, pp. 292-298, 2012.

[36] A. Häggkvist, J. Sjöström and U. Wickström, "Using plate thermometer measurements to calculate incident heat radiation," *Journal Of Fire Sciences*, vol. 31, no. 2, pp. 166-177, 2013.

[37] A. Grine, J. Desmons and S. Harmand, "Models for transient conduction in a flat plate subjected to a variable heat flux," *Applied Thermal Engineering*, vol. 27, no. 2/3, pp. 492-500, 2007.

[38] W. Mansur, C. Vasconcellos, N. Zambrozuski and O. R. Filho, "Numerical solution for the linear transient heat conduction equation using an Explicit Green's Approach," *International Journal of Heat and Mass Transfer*, vol. 52, no. 3-4, pp. 694-701, 2009.

[39] A. Sutradhar, G. H. Paulino and L. J. Gray, "Transient heat conduction in homogeneous and non-homogeneous materials by the Laplace transform Galerkin boundary element method," *Engineering Analysis With Boundary Elements*, vol. 26, no. 2, pp. 119-233, 2002.

[40] N. Sahoo and R. K. Peetala, "Transient surface heating rates from a nickel film sensor using inverse analysis," *International Journal of Heat and Mass Transfer*, vol. 54, no. 5-6, pp. 1297-1302, 2011.

[41] C.-L. Fu, X.-T. Xiong and P. Fu, "Fourier regularization method for solving the surface heat flux from interior observations," *Mathematical and Computer Modelling*, vol. 42, no. 5-6, pp. 489-498, 2005.

[42] A. Fernandes, P. Sousa, V. Borges and G. Guimaraes, "Use of 3D-transient analytical solution based on Green's function to reduce computational time in inverse heat conduction problems," *Applied Mathematical Modelling*, vol. 34, no. 12, pp. 4040-4049, 2010.

[43] A. Bova and M. Dickinson, "An inverse method to estimate stem surface heat flux in wildland fires," *International Journal Of Wildland Fire*, vol. 18, no. 6, pp. 711-721, 2009.

[44] Y. A. Çengel and A. J. Ghajar, Heat and Mass Transfer: Fundamentals & Applications, 4th ed., New York: McGraw-Hill, 2011, pp. 237, 249, 527, 753, 884.

[45] M. Özışık, Heat conduction, New York: Wiley, 1980, pp. 18-20, 34-37.

[46] T. Threlfall, "Comparison of Common Heat Flux Gauge Results," Saskatoon, University of Saskatchewan, 2003, pp. 1-37.

[47] H. S. Carslaw and J. C. Jaeger, Conduction of heat in solids, 2nd ed., Oxford: Clarendon Press, 1959, pp. 112-114.

[48] S. Liodakis, D. Vorisis and I. P. Agiovlasitis, "Testing the retardancy effect of various inorganic chemicals on smoldering combustion of Pinus halepensis needles," *Thermochimica Acta* , vol. 444, no. 2, pp. 157-165, 2006.

[49] C. Hogue, "Seeing red. (red-tinted fire retardants for fighting wildfires," *Chemical & Engineering News,* vol. 89, no. 35, pp. 11-15, 29 August 2011.

[50] A. Gimenez, E. Pastor, L. Zarate, E. Planas and J. Arnaldos, "Long-term forest fire retardants: a review of quality, effectiveness, application and environmental considerations," *International Journal of Wildland Fire,* vol. 13, no. 1, pp. 1-15, 2004.

[51] S. Liodakis, V. Tsapara, I. Agiovlasitis and D. Vorisis, "Thermal analysis of Pinus sylvestris L. wood samples treated with a new gel-mineral mixture of short- and long-term fire retardants.," *Thermochimica Acta,* vol. 568, pp. 156-160, 2013.

[52] "Specification for Long Term Retardant, Wildland Firefighting," United States Department of Agriculture Forest Service: Specification 5100-304c, 2010, pp. 1-2.

[53] L. Jiji, Heat Conduction, 2nd ed., New York: Begell House, Inc., 2003, pp. 82-83, 402-404.

[54] G. Nellis and S. A. Klein, Heat Transfer, New York: Cambridge University Press, 2009, pp. 5-9.

[55] L. Jiji, Heat Convection, 2nd ed., Berlin: Springer, 2009, pp. 6, 260-279.

[56] X. Silvani and F. Morandini, "Fire spread experiments in the field: Temperature and heat flux measurements," *Fire Safety Journal*, vol. 44, no. 2, pp. 279-285, 2009.

[57] F. Cardarelli, Materials handbook: a concise desktop reference, London: Springer, 2008, p. 174.

[58] J. Bray, "Aluminum Mill and Engineered Wrought Products, Properties and Selection: Nonferrous Alloys and Special-Purpose Materials," in *ASM Handbook*, vol. 2, ASM International, 1990, pp. 29-61.

[59] Y. S. Touloukian, Thermophysical properties of matter: Thermal Conductivity: Metallic Elements and Alloys, New York: IFI/Plenum, 1970, pp. 1, 908-909.

[60] HukseфluxUSA Inc., "SBG01 Water Cooled Heat Flux Sensor According to Schmidt-Boelter," Manorville, Hukseflux Inc.: Specifications Brochure Version 1109, 2008, pp. 1-2.

[61] Sequoia Technologies, "Heat Flux Sensors for Measurement of Conductive, Radiative and Convective," [Online]. Available: http://www.sequoia.co.uk/division.php?id=2. [Accessed 10 January 2014].

[62] Medtherm, "Bulletin 118: Heat Flux Transducers and Infrared Radiometers for the Direct Measurement of Heat Transfer Rates," Huntsville, Medtherm Corporation, 2013, pp. 1-4.

[63] V. Peridier, "Estimating Transient Sruface Heating using a Cellular Automation Energy-transport Model," *Complex Systems -Champaign-*, vol. 16, no. 2, pp. 139-154, 2006.

[64] Stirling Consolidated Boiler Company, A Book on Steam for Engineers, New York: The Stirling Company, 1905, p. 50.

[65] A. McDonald, C. Moreau and S. Chandra, "Use of thermal emission signals to characterize the impact of fully and partially molten plasma-sprayed zirconia particles on glass surfaces," *Surface & Coatings Technology*, vol. 204, no. 15, pp. 2323-2330, 2010.

[66] A. McDonald, C. Moreau and S. Chandra, "Thermal contact resistance between plasma-sprayed particles and flat surfaces," *International Journal Of Heat And Mass Transfer*, vol. 50, no. 9-10, pp. 1737-1749, 2007.

[67] R. Ault, M. Ackerman and G. Dakin, "Development of a Test Method for the Effectiveness of Gels and Retardants for Delaying Ignition of Forest Fuels," Edmonton, FP Innovations, 2013, pp. 1-38.

[68] Omega Engineering Incorporated, *ANSI and IEC Color Codes for Thermocouples, Wire, and Connectors*, Stamford, 2004, pp. H3-H9.

[69] J. R. Taylor, An Introduction to Error Analysis: The Study of Uncertainties in Physical Measurements, 2nd ed., Sausalito: University Science Books, 1996, pp. 13, 60-66.

[70] ISO (International Organization for Standardization), "Fire Tests - Calibration and use of heat flux meters - Part 2: Preliminary calibration methods," ISO 14934-2:2013, 2013, pp. 1-46.

APPENDIX A – ENGINEERED DRAWING OF HEAT FLUX SENSOR

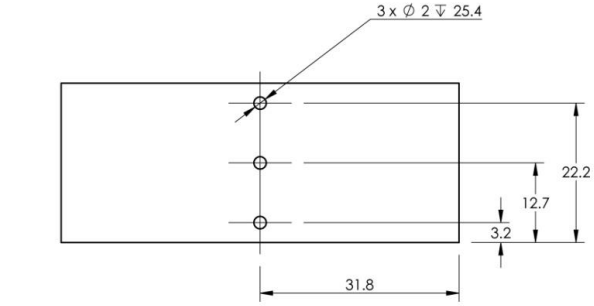

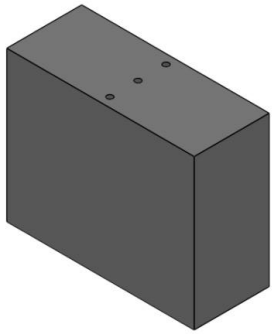

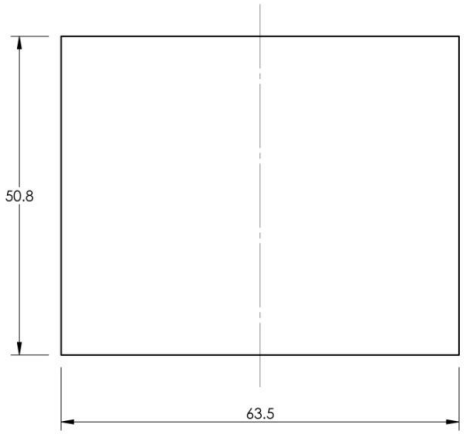

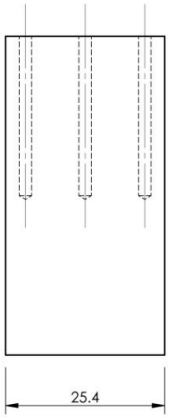

Instructor: Fall 2013 Comments:	UNLESS OTHERWISE SPECIFIED: DIMENSIONS ARE IN MM TOLERANCES: ANGULAR: ± 0.5° LINEAR X = ± 0.5 X.X = ± 0.1 X.XX = ± 0.025 SURFACE FINISH µm 0.6 DO NOT SCALE DRAWING	DRAWN BY: Erik Sullivan Student # 1222809 Lab Day SM By Erik Sullivan TA Initials	The Department of Mechanical Engineering UNIVERSITY OF ALBERTA TITLE: Thermal Cube
MATERIAL: 6063-T4 FILE NAME: Aluminum Block (with holes) 2		Tuesday, October 22, 2013 2:23:10 PM Tuesday, April 30, 2013 10:50:09 AM	SIZE B · Assignment Number · REV SCALE: 2:1 · Mass: 0.49 · SHEET 1 OF 1

APPENDIX B – WILDFIRE SUPPRESSION CHEMICAL SPECIFICATION SHEET

REPRINTED WITH PERMISSION

PHOS-CHEK®

Fire Retardant, Class A Foam & Gel

ICL Performance Products LP

www.phoschek.com

PHOS-CHEK® LC-95 Fire Retardants

Low Viscosity Liquid Concentrate

Uses:

PHOS-CHEK LC-95 Fire Retardants are qualified by the USDA Forest Service for use in fixed-wing air tankers and helicopters with buckets and ground engines. LC-95 is ideal for use in multi-engine fixed-wing air tankers, single engine air-tankers (SEATS). The concentrate is delivered to the using location as a low viscosity liquid and is stored in the concentrate form. It is diluted and mixed with water as it is transferred to the delivery system.

PHOS-CHEK Fire Retardants are used for wildland fire control in forest, brush or grassland. Functionally, PHOS-CHEK Retardants react with and alter the thermal decomposition of wildland fuels so that they do not support flaming or glowing combustion. This deprives the fire of fuel reducing fire intensity and the rate of flame spread. They are useful as well in prescribed burning. When applied at low application rates, fire intensity is dramatically decreased while slow burning is allowed.

Description:

PHOS-CHEK LC-95 Fire Retardants are concentrated liquids that mix readily with water by recirculation, agitation or mechanical or electronic PHOS-CHEK liquid proportioning systems. PHOS-CHEK LC-95 fire retardant solutions are the only liquid concentrate (LC) ammonium polyphosphate retardants that offer both the ease of mixing and handling of a liquid and the aerial drop advantages of a gum-thickened retardant. The elastic nature of the thickener in PHOS-CHEK retardants facilitates increased fuel coverage, wrap around and penetration through canopy and ladder fuels to ground vegetation.

Both LC-95A and LC-95D are red iron oxide colored. All PHOS-CHEK retardants are the most environmentally friendly retardants available.

Typical Analysis:

Color:	Red (R)
Mix Ratio:	LC-95A - 5.5 volumes of water per volume concentrate LC-95D - 4.25 volumes of water per volume concentrate
Yield:	LC-95A - 1054 US gals per ton concentrate *(4398 liters / MT)* 6.47 volumes of dilute per volume concentrate LC-95D - 869 US gals per ton concentrate *(3626 liters / MT)* 5.21 volumes of dilute per volume concentrate
Density:	LC-95A - 12.28 lbs per US gallon concentrate *(1.476 kg per liter)* 8.97 lbs per US gallon of dilute *(1.078 kg per liter)* LC-95D - 11.99 lbs per US gallon concentrate *(1.441 kg per liter)* 9.09 lbs per US gallon of dilute *(1.092 kg per liter)*
Viscosity:	100-200 centipoise (cP)

Packaging:

PHOS-CHEK LC-95 is available in bulk trucks, 260 and 330 gallon totes, 30 and 55 gallon drums and 5 gallon pails. Special packaging available.

PHOS-CHEK®

Fire Retardant, Class A Foam & Gel

ICL Performance Products LP

www.phoschek.com

PHOS-CHEK® LC-95 Fire Retardants

Low Viscosity Liquid Concentrate

Handling Precautions:

FOR DETAILED SAFETY INFORMATION PLEASE REFER TO THE MSDS.

MAY CAUSE IRRITATION TO EYES; CONSIDERED PRACTICALLY NO IRRITATION TO SKIN.

PRECAUTIONARY MEASURE AND FIRST-AID HANDLE IN ACCORDANCE WITH GOOD INDUSTRIAL HYGIENE AND SAFETY PRACTICES. THESE PRACTICES INCLUDE AVOIDING UNNECESSARY CONTACT AND REMOVAL OF THE MATERIAL FROM THE EYES, SKIN AND CLOTHING.

EYE PROTECTION: As a good industrial practice, the use of chemical goggles is recommended. Eye flushing equipment should also be available.

SKIN PROTECTION: Wear protective gloves to minimize skin contact. Wash hands and contaminated skin after handling.

RESPIRATORY PROTECTION: None required.

IF IN EYES: Flush with plenty of water.

For more information, contact any of our worldwide wildfire offices or visit us at www.phoschek.com:

United States
ICL Performance Products LP
810 E. Main St.
Ontario, CA 91761
Tel (800) 682-3626
(909) 983-0772
24 Hrs (909) 946-7371
Fax (909) 984-4770

Canada
ICL Performance Products
Canada LTD
3060 Airport Road
Kamloops, BC
Canada, V2B 7X2
Tel (800) 665-2535
(250) 554-3530
Fax (250) 554-7788

Europe
Biogema
415, rue Armand-Pole
d'Activities
13852 Aix-en-Provence Cedex 3
France
Tel (0) 4 42 24 45 08
Fax (0) 4 42 24 29 98

Australia
Phoz-Chem Pty Ltd.
P.O. Box 2034
Templestowe Hts. Vic 3107
Australia
Tel 61 3 9848 1111
Fax 61 3 9848 2711